Real-time phase-resolved ocean wave prediction in directional wave fields: Second-order Lagrangian wave models

I.-C. Kim, Guillaume Ducrozet

Ocean Engineering 313 (2024) 119316

Contents lists available at ScienceDirect

Ocean Engineering

journal homepage: www.elsevier.com/locate/oceaneng

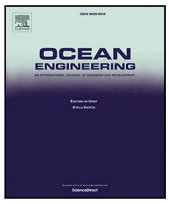

Research paper

Real-time phase-resolved ocean wave prediction in directional wave fields: Second-order Lagrangian wave models

I.-C. Kim [a,b,*], G. Ducrozet [a]

[a] Nantes Université, École Centrale Nantes, CNRS, LHEEA, UMR 6598, F-44000 Nantes, France
[b] College of Earth, Ocean, and Atmospheric Sciences, Oregon State University, Corvallis, OR, USA

ARTICLE INFO

Dataset link: https://doi.org/10.5281/zenodo.7689781

Keywords:
Ocean waves
Phase-resolved model
Real-time prediction
Directional wave
Wave tank experiments

ABSTRACT

The Improved Choppy Wave Model (ICWM) was established to achieve a second-order Lagrangian expansion of surface waves. The second-order Lagrangian nonlinear interaction terms were found to be negligible and were therefore discarded. However, these interactions in directional wave fields remained unexplored. ICWM was successfully used, especially for floating offshore wind turbines, but it was noted that its accuracy in predicting directional sea states needed improvement. Hence, we formulated the Complementary ICWM (CICWM) with the nonlinear terms for free surface elevation in directional waves. Detailed formulations for data assimilation and wave propagation were provided, enabling real-time wave forecasting for directional seas using a simplified assimilation method. Comparing the model performances against tank-scale experiments showed that CICWM enhances the surface elevation description in directional seas. Ultimately, it was confirmed that the second-order Lagrangian model can reduce the prediction error of the linear wave model by 90% in directional seas for the experimental setups and sea states investigated in this study.

1. Introduction

The real-time prediction of deterministic ocean wave surfaces is of great importance in marine science and ocean engineering. The safe and efficient operation of surface vessels involves predicting ocean waves for future scenarios (Grilli et al. 2011, Nouguier et al. 2013, Kusters et al. 2016, Dannenberg et al. 2010). Similarly, the availability of real-time short-term phase-resolved sea wave prediction is a central challenge for ocean renewable energy harvesting systems (Li et al. 2012, Previsic et al. 2021) and the operational performance of marine structures, such as floating offshore wind turbines (Raach et al. 2014, Ma et al. 2018, Al et al. 2020). Recently, Kim et al. (2024b) validated deterministic predictions of both ocean wave elevations and excitation forces on the floating body against dedicated tank-scale experiments in directional sea states.

Optical sensor systems, such as LIDAR (Light Detection and Ranging) cameras (Grilli et al. 2011, Nouguier et al. 2013, Kabel et al. 2019), and X-band radars (Hilmer and Thornhill 2015, Kusters et al. 2016, Naaijen et al. 2018, Klein et al. 2020, Zhang et al. 2022), are employed to collect sea surface elevation data for developing phase-resolved ocean wave forecasts. While these systems capture extensive domains of ocean surface wave fields, the spatial density of measurement points decreases geometrically with distance from the sensor due to its aperture angles. Moreover, spatial gaps behind illuminated wavefronts induce wave shadowing effects, causing a more uneven distribution of wave elevation points in space. To overcome this challenge, including the shadowing effects, spatio-temporal data sets can be used, enabling the detection of ocean surface points surrounding the camera under shadows at a later time (e.g., Grilli et al. 2011, Nouguier et al. 2013, Kabel et al. 2019, Desmars et al. 2020).

Understanding the instantaneous state of nonlinear wave motions is crucial for an accurate description of ocean surface elevations over a long forecast horizon in time and/or in significantly nonlinear sea states. The Lagrangian approach appears particularly attractive in the study of surface gravity wave simulations at high orders of wave steepness (Socquet-Juglard et al. 2005, Lindgren 2006, Clamond 2007 among others). The Lagrangian representation excels in describing steep waves and assessing statistical and geometrical quantities in random wave fields at a reduced numerical expense (Lindgren and Åberg, 2009). Consequently, several authors have proposed real-time wave prediction algorithms through nonlinear phase-resolved wave models based on Lagrangian descriptions that incorporate essential nonlinear effects (e.g., Grilli et al. 2011, Nouguier et al. 2013, Desmars et al. 2023).

Gerstner (1809) explicitly developed a first-order solution to a periodic evolution of Lagrangian wave particles. Pierson (1961) introduced a solution to complete dynamical Lagrangian equations among

* Corresponding author at: College of Earth, Ocean, and Atmospheric Sciences, Oregon State University, Corvallis, OR, USA.
E-mail address: inchul.kim@oregonstate.edu (I.-C. Kim).

https://doi.org/10.1016/j.oceaneng.2024.119316
Received 14 May 2024; Received in revised form 28 August 2024; Accepted 18 September 2024
Available online 27 September 2024

multiple surface gravity waves. Nouguier et al. (2009), extending the model of Gerstner (1809) to two-dimensional surfaces, developed a numerically efficient and nonlinearly robust wave model, known as the Choppy Wave Model (CWM), based on the small displacements of Lagrangian first-order particles. The subsequent development of a complete second-order version of CWM, referred to as CWM2, was carried out by Nouguier et al. (2015). Applying a perturbation expansion approach as described by Stoker (1992), they developed exact solutions based on the fundamental equation for fluid particle motion (Lamb, 1932). This version ensured the inclusion of additional nonlinear effects up to the second order in the Lagrangian solution. Nouguier et al. (2015) demonstrated the consistency of CWM2 with the second-order classical Eulerian model of Longuet-Higgins (1963). While the first-order approximation (i.e., CWM) does not align entirely with the classical Eulerian approach, the second-order version exhibits perfect consistency. Additionally, they showed that CWM2 achieves improvements in terms of the mean sea level compared to the classical Lagrangian expansion of Pierson (1961).

Guérin et al. (2019) thereafter demonstrated that retaining selected nonlinear properties, such as Stokes drift and mean vertical level, not only improves numerical efficiency but also maintains forecast accuracy via a simplified model, namely, the Improved Choppy Wave Model (ICWM). More importantly, the use of a redefinition of reference particles circumvents problems associated with increasing phase shifts (or discrepancies with the nonlinear wave dispersion relationship). Recently, this Lagrangian wave model has proven to be well-suited for accomplishing real-time phase-resolved ocean wave predictions with great accuracy and efficiency in unidirectional wave fields (Desmars et al. 2020, 2023), multidirectional wave fields (Kim et al., 2023a), and operational scenarios (Kim et al., 2024a).

More specifically, in comparison to the earlier model CWM2, ICWM omits nonlinear second-order Lagrangian interaction terms, except for those occurring between identical modes in frequency and direction (or the mean vertical level terms). Guérin et al. (2019) explored the effects of these omitted interaction terms by comparing ICWM with ICWM including the second-order interaction terms (Complementary ICWM, CICWM), against a synthetic reference dataset for long-crested waves. They found that these nonlinear terms are significant only during a short period and become increasingly negligible over time in the evolution of random nonlinear surface waves in unidirectional cases.

However, within the context of feed-forward wave-based controllers for floating offshore wind turbines, a short time horizon of wave prediction is crucial, as the forecast accuracy of the wave excitation forces highly depends on short-term deterministic wave prediction (Guo et al. 2017, Al et al. 2020, Kim et al. 2024b). Additionally, Kim et al. (2023a) reported that in their short-term wave forecasting, while the effect of nonlinear phase shift is similarly crucial in both unidirectional and directional cases, the Stokes drift effect in directional cases is not as significant as in unidirectional cases. Consequently, the improvement by ICWM in comparison to the linear model is less pronounced for directional seas. This difference likely arises because the nonlinear phase shift and the Stokes drift operate at second order and third order in wave steepness, respectively. Therefore, aiming to increase the gap between the nonlinear and linear models over the short-term forecast, especially in directional scenarios, we extend the method of Kim et al. (2023a) by incorporating the second-order Lagrangian interaction terms.

First, we propose an explicit formulation of CICWM for the free surface elevation, considering all combinations between aligned and non-aligned wave vector components in three-dimensional random wave systems. Subsequently, we validate the wave prediction algorithm based on CICWM against dedicated tank-scale experiments. The inclusion of directional modes complicates and enhances nonlinear wave-wave interactions, potentially leading to energy redistribution across a broad range of directions (Janssen et al., 2006). However, these nonlinear interactions may hinder the complementary model from achieving real-time capabilities, particularly in multidirectional cases. Hence, we develop algorithms for real-time ocean wave prediction using a simplified assimilation method suggested in Kim et al. (2023a).

The paper is organized as follows. Section 2 outlines the derivation of an explicit formulation of CICWM for the free surface elevation, followed by the algorithms for real-time phase-resolved ocean wave forecasting provided in Section 3. In particular, Section 3.1 offers a comprehensive overview of the wave models employed in this study in the order of their development. Section 4 explains the experimental data. The numerical simulations of the wave models are compared with the experimental observations in Section 5. Lastly, the conclusions of the present study are detailed in Section 6. Additional details regarding the derivation of the simplified version of ICWM (SICWM) and data assimilation, are given respectively in Appendices A and B.

2. Derivation of equations

2.1. Lagrangian evolution equations

Based on the Lagrangian form in Lamb (1932), Nouguier et al. (2015) obtained a second-order solution to the motion of fluid particles using the usual perturbation technique. Similarly, Guérin et al. (2019) sought a perturbation expansion in the second order of wave steepness from the Eulerian velocity field described by Longuet-Higgins (1963). For an inviscid, incompressible, and irrotational fluid, the particle trajectories at time t around the modified reference location $(\bar{x}, \bar{y}, \bar{z})$ for a discrete short-crested sea state are presented in Guérin et al. (2019) (see the appendix in their published literature):

$$\begin{aligned} x(t) &= \bar{x} + x_1(t) + x_2(t) \\ y(t) &= \bar{y} + y_1(t) + y_2(t) \\ z(t) &= \bar{z} + z_1(t) + z_2(t) \end{aligned} \tag{1}$$

where $\mathbf{r} = (x, y)$ represents the horizontal components of particle position, with z being positive in the vertical upward direction. The first-order particle fluctuations are

$$x_1 = \sum_{i_\omega=1}^{N_\omega} \sum_{i_\theta=1}^{N_\theta} A_{(i_\omega,i_\theta)} e^{k_{i_\omega}\bar{z}} \cos\theta_{i_\theta} \sin\bar{\psi}_{(i_\omega,i_\theta)} = \sum_{i=1}^{N} A_i e^{k_i\bar{z}} \frac{k_{i_x}}{k_i} \sin\bar{\psi}_i \tag{2}$$

$$y_1 = \sum_{i_\omega=1}^{N_\omega} \sum_{i_\theta=1}^{N_\theta} A_{(i_\omega,i_\theta)} e^{k_{i_\omega}\bar{z}} \sin\theta_{i_\theta} \sin\bar{\psi}_{(i_\omega,i_\theta)} = \sum_{i=1}^{N} A_i e^{k_i\bar{z}} \frac{k_{i_y}}{k_i} \sin\bar{\psi}_i \tag{3}$$

$$z_1 = \sum_{i_\omega=1}^{N_\omega} \sum_{i_\theta=1}^{N_\theta} A_{(i_\omega,i_\theta)} e^{k_i\bar{z}} \cos\bar{\psi}_{(i_\omega,i_\theta)} = \sum_{i=1}^{N} A_i e^{k_i\bar{z}} \cos\bar{\psi}_i \tag{4}$$

where A_i denotes the amplitude, and the subscript $i = (i_\omega, i_\theta)$ refers to the ith wave component, with indices for the frequency component i_ω and for the direction component i_θ. Henceforth, we opted to use the index vector i in formulating the equations rather than the component indices i_ω and i_θ, primarily due to the increased complexity arising from the inclusion of second-order terms. The total number of wave components is $N = N_\omega \times N_\theta$, with N_ω and N_θ the total numbers of wave components in frequency and direction, respectively. The wavenumber vector $\mathbf{k}_i = (k_{i_x}, k_{i_y})$ is given by the wavenumber k_i and the propagating direction θ_i, i.e. $k_{i_x} = k_i \cos\theta_i$ and $k_{i_y} = k_i \sin\theta_i$. The phase function at the reference location $\bar{\mathbf{r}} = (\bar{x}, \bar{y})$ is

$$\bar{\psi}_i = \mathbf{k}_i \cdot \bar{\mathbf{r}} - \omega_i t - \varphi_i = k_i \cos\theta_i \bar{x} + k_i \sin\theta_i \bar{y} - \omega_i t - \varphi_i \tag{5}$$

in which the wave frequency ω_i is given by the linear dispersion relation for gravity waves in deep water, and φ_i is the random phase. A comparable equation can be readily derived using the fully dispersive wavenumber for a finite water depth.

Next, for the second-order contributions for three-dimensional irregular waves, only the time derivatives of particle location (or the Lagrangian velocities) are provided in Guérin et al. (2019); therefore,

further algebraic processing is necessary to obtain the second-order fluctuations:

$$
\begin{aligned}
x_2 = {} & \frac{1}{2}\sum_{i,j} A_i A_j \begin{bmatrix} e^{|\mathbf{k}_i-\mathbf{k}_j|\bar{z}}\mathcal{B}_{ij}^{-}\left(-\frac{k_{i_x}-k_{j_x}}{\omega_i-\omega_j}\right)\sin\left(\bar{\psi}_i-\bar{\psi}_j\right) \\ +e^{|\mathbf{k}_i+\mathbf{k}_j|\bar{z}}\mathcal{B}_{ij}^{+}\left(-\frac{k_{i_x}+k_{j_x}}{\omega_i+\omega_j}\right)\sin\left(\bar{\psi}_i+\bar{\psi}_j\right) \end{bmatrix} \\
& + \frac{1}{2}\sum_{j_\omega\neq i_\omega} A_i A_j e^{(k_i+k_j)\bar{z}} \begin{bmatrix} -\left(\frac{k_{i_x}\omega_i+k_{j_x}\omega_j}{\omega_i-\omega_j}\right)\left(\frac{\mathbf{k}_i\cdot\mathbf{k}_j}{2k_ik_j}+\frac{1}{2}\right)\sin\left(\bar{\psi}_i-\bar{\psi}_j\right) \\ -\left(\frac{k_{i_x}\omega_i+k_{j_x}\omega_j}{\omega_i+\omega_j}\right)\left(-\frac{\mathbf{k}_i\cdot\mathbf{k}_j}{2k_ik_j}+\frac{1}{2}\right)\sin\left(\bar{\psi}_i+\bar{\psi}_j\right) \end{bmatrix} \\
& + \frac{1}{2}\sum_{\substack{j_\omega=i_\omega \\ j_\theta\neq i_\theta}} A_i A_j e^{(k_i+k_j)\bar{z}} \left[\left(k_{i_x}\omega_i+k_{j_x}\omega_j\right)\left(\frac{\mathbf{k}_i\cdot\mathbf{k}_j}{2k_ik_j}+\frac{1}{2}\right)\cos\left(\bar{\psi}_i-\bar{\psi}_j\right)\right]t \\
& + \sum_i {A_i}^2 e^{2k_i\bar{z}} k_{i_x}\omega_i t + C_x
\end{aligned}
\tag{6}
$$

$$
\begin{aligned}
y_2 = {} & \frac{1}{2}\sum_{i,j} A_i A_j \begin{bmatrix} e^{|\mathbf{k}_i-\mathbf{k}_j|\bar{z}}\mathcal{B}_{ij}^{-}\left(-\frac{k_{i_y}-k_{j_y}}{\omega_i-\omega_j}\right)\sin\left(\bar{\psi}_i-\bar{\psi}_j\right) \\ +e^{|\mathbf{k}_i+\mathbf{k}_j|\bar{z}}\mathcal{B}_{ij}^{+}\left(-\frac{k_{i_y}+k_{j_y}}{\omega_i+\omega_j}\right)\sin\left(\bar{\psi}_i+\bar{\psi}_j\right) \end{bmatrix} \\
& + \frac{1}{2}\sum_{j_\omega\neq i_\omega} A_i A_j e^{(k_i+k_j)\bar{z}} \begin{bmatrix} -\left(\frac{k_{i_y}\omega_i+k_{j_y}\omega_j}{\omega_i-\omega_j}\right)\left(\frac{\mathbf{k}_i\cdot\mathbf{k}_j}{2k_ik_j}+\frac{1}{2}\right)\sin\left(\bar{\psi}_i-\bar{\psi}_j\right) \\ -\left(\frac{k_{i_y}\omega_i+k_{j_y}\omega_j}{\omega_i+\omega_j}\right)\left(-\frac{\mathbf{k}_i\cdot\mathbf{k}_j}{2k_ik_j}+\frac{1}{2}\right)\sin\left(\bar{\psi}_i+\bar{\psi}_j\right) \end{bmatrix} \\
& + \frac{1}{2}\sum_{\substack{j_\omega=i_\omega \\ j_\theta\neq i_\theta}} A_i A_j e^{(k_i+k_j)\bar{z}} \left[\left(k_{i_y}\omega_i+k_{j_y}\omega_j\right)\left(\frac{\mathbf{k}_i\cdot\mathbf{k}_j}{2k_ik_j}+\frac{1}{2}\right)\cos\left(\bar{\psi}_i-\bar{\psi}_j\right)\right]t \\
& + \sum_i {A_i}^2 e^{2k_i\bar{z}} k_{i_y}\omega_i t + C_y
\end{aligned}
\tag{7}
$$

$$
\begin{aligned}
z_2 = {} & \frac{1}{2}\sum_{i,j} A_i A_j \begin{bmatrix} e^{|\mathbf{k}_i-\mathbf{k}_j|\bar{z}}\mathcal{B}_{ij}^{-}\frac{|\mathbf{k}_i-\mathbf{k}_j|}{\omega_i-\omega_j}\cos\left(\bar{\psi}_i-\bar{\psi}_j\right) \\ +e^{|\mathbf{k}_i+\mathbf{k}_j|\bar{z}}\mathcal{B}_{ij}^{+}\frac{|\mathbf{k}_i+\mathbf{k}_j|}{\omega_i+\omega_j}\cos\left(\bar{\psi}_i+\bar{\psi}_j\right) \end{bmatrix} \\
& + \frac{1}{2}\sum_{j_\omega\neq i_\omega} A_i A_j e^{(k_i+k_j)\bar{z}} \begin{bmatrix} \left(\frac{k_i\omega_i-k_j\omega_j}{\omega_i-\omega_j}\right)\left(\frac{\mathbf{k}_i\cdot\mathbf{k}_j}{2k_ik_j}+\frac{1}{2}\right)\cos\left(\bar{\psi}_i-\bar{\psi}_j\right) \\ +\left(\frac{k_i\omega_i+k_j\omega_j}{\omega_i+\omega_j}\right)\left(-\frac{\mathbf{k}_i\cdot\mathbf{k}_j}{2k_ik_j}+\frac{1}{2}\right)\cos\left(\bar{\psi}_i+\bar{\psi}_j\right) \end{bmatrix} \\
& + \frac{1}{2}\sum_{\substack{j_\omega=i_\omega \\ j_\theta\neq i_\theta}} A_i A_j e^{(k_i+k_j)\bar{z}} \left[\left(\frac{k_i\omega_i+k_j\omega_j}{\omega_i+\omega_j}\right)\left(-\frac{\mathbf{k}_i\cdot\mathbf{k}_j}{2k_ik_j}+\frac{1}{2}\right)\cos\left(\bar{\psi}_i+\bar{\psi}_j\right)\right] + C_z
\end{aligned}
\tag{8}
$$

where $i=(i_\omega,i_\theta)$ and $j=(j_\omega,j_\theta)$ are two arbitrary modes, C_x, C_y, and C_z are the constants of time integration, and the interaction coefficients $\mathcal{B}_{ij}^{\mp}$ are

$$
\begin{aligned}
\mathcal{B}_{ij}^{-} &= \frac{\omega_i\omega_j}{k_ik_j}\frac{\left(\omega_i-\omega_j\right)\left(\mathbf{k}_i\cdot\mathbf{k}_j+k_ik_j\right)}{\left(\omega_i-\omega_j\right)^2-g\left|\mathbf{k}_i-\mathbf{k}_j\right|} \\
\mathcal{B}_{ij}^{+} &= \frac{\omega_i\omega_j}{k_ik_j}\frac{\left(\omega_i+\omega_j\right)\left(\mathbf{k}_i\cdot\mathbf{k}_j-k_ik_j\right)}{\left(\omega_i+\omega_j\right)^2-g\left|\mathbf{k}_i+\mathbf{k}_j\right|}
\end{aligned}
\tag{9}
$$

with $\mathcal{B}_{ij}^{-}=0$ for $i_\omega=j_\omega$ and $\mathcal{B}_{ij}^{+}=0$ for $i_\theta=j_\theta$. Following Guérin et al. (2019), the horizontal constants are selected as

$$
\begin{aligned}
C_x &= -\frac{1}{2}\sum_i {A_i}^2 e^{2k_i\bar{z}}\omega_i k_{i_x} t \\
C_y &= -\frac{1}{2}\sum_i {A_i}^2 e^{2k_i\bar{z}}\omega_i k_{i_y} t
\end{aligned}
\tag{10}
$$

with $C_z=0$ and $\bar{z}=\frac{1}{2}\sum_i {A_i}^2 k_i$ leads to the zero mean vertical position.

The interaction coefficients $\mathcal{B}_{ij}^{\mp}$ are denoted as $A_{ij}^{\mp}$ in Guérin et al. (2019) (see equation (A4) in their paper). We have made corrections to the interaction coefficients (Eq. (9)) and the second-order solution (Eqs. (6), (7), and (8); see the appendix of their work) to ensure consistency with formulations in a unidirectional case. For example, the factor of 1/2 will be canceled out when splitting double summations with a condition of $j_\omega > i_\omega$ or $j_\theta > i_\theta$. Additionally, the signs in Eq. (9) are opposite to those in the publication, resulting in terms that account for the sum interactions of two wave components (i.e., proportional to $\mathcal{B}_{ij}^{+}$) disappearing in a unidirectional case. These discrepancies are thus regarded as misprints in their work.

2.2. Free surface elevation

Ocean surface measurements, typically obtained through optical systems, are collected at irregularly distributed locations within a predefined reference coordinate system, namely, a Eulerian system. Consequently, the direct application of the Lagrangian form in the previous section is not feasible. As in previous studies such as Nouguier et al. (2009) and Desmars et al. (2020), we derive an approximate model within a formalism of free surface elevation in this section.

After substituting Eqs. (2) through (4) and (6) through (8) into Eq. (1) and utilizing the aforementioned constants, vertical reference location, and implementing some algebraic simplifications, the complete particle location up to second order is obtained in directional sea states:

$$
\begin{aligned}
\mathbf{r} = {} & \bar{\mathbf{r}} - \sum_{i=1}^{N} A_i\frac{\mathbf{k}_i}{k_i}\sin\bar{\psi}_i \\
& + \sum_{j_\omega>i_\omega} A_i A_j \begin{bmatrix} \left\{\mathcal{B}_{ij}^{-}\left(-\frac{\mathbf{k}_i-\mathbf{k}_j}{\omega_i-\omega_j}\right)-\left(\frac{\mathbf{k}_i\omega_i+\mathbf{k}_j\omega_j}{\omega_i-\omega_j}\right)\left(\frac{\mathbf{k}_i\cdot\mathbf{k}_j}{2k_ik_j}+\frac{1}{2}\right)\right\}\sin\left(\bar{\psi}_i-\bar{\psi}_j\right) \\ +\left\{\mathcal{B}_{ij}^{+}\left(-\frac{\mathbf{k}_i+\mathbf{k}_j}{\omega_i+\omega_j}\right)-\left(\frac{\mathbf{k}_i\omega_i+\mathbf{k}_j\omega_j}{\omega_i+\omega_j}\right)\left(-\frac{\mathbf{k}_i\cdot\mathbf{k}_j}{2k_ik_j}+\frac{1}{2}\right)\right\}\sin\left(\bar{\psi}_i+\bar{\psi}_j\right) \end{bmatrix} \\
& + \sum_{\substack{j_\omega=i_\omega \\ j_\theta>i_\theta}} A_i A_j \left\{\mathcal{B}_{ij}^{+}\left(-\frac{\mathbf{k}_i+\mathbf{k}_j}{\omega_i+\omega_j}\right)-\left(\frac{\mathbf{k}_i\omega_i+\mathbf{k}_j\omega_j}{\omega_i+\omega_j}\right)\left(-\frac{\mathbf{k}_i\cdot\mathbf{k}_j}{2k_ik_j}+\frac{1}{2}\right)\right\}\sin\left(\bar{\psi}_i+\bar{\psi}_j\right) \\
& + \sum_{\substack{j_\omega=i_\omega \\ j_\theta>i_\theta}} A_i A_j \left[\left(\mathbf{k}_i\omega_i+\mathbf{k}_j\omega_j\right)\left(\frac{\mathbf{k}_i\cdot\mathbf{k}_j}{2k_ik_j}+\frac{1}{2}\right)\cos\left(\bar{\psi}_i-\bar{\psi}_j\right)\right]t + \frac{1}{2}\sum_{i=j} {A_i}^2\mathbf{k}_i\omega_i t
\end{aligned}
\tag{11}
$$

$$
\begin{aligned}
z = {} & \frac{1}{2}\sum_{i=1}^{N} {A_i}^2 k_i + \sum_{i=1}^{N} A_i\cos\bar{\psi}_i \\
& + \sum_{j_\omega>i_\omega} A_i A_j \begin{bmatrix} \left\{\mathcal{B}_{ij}^{-}\frac{|\mathbf{k}_i-\mathbf{k}_j|}{\omega_i-\omega_j}+\left(\frac{k_i\omega_i-k_j\omega_j}{\omega_i-\omega_j}\right)\left(\frac{\mathbf{k}_i\cdot\mathbf{k}_j}{2k_ik_j}+\frac{1}{2}\right)\right\}\cos\left(\bar{\psi}_i-\bar{\psi}_j\right) \\ +\left\{\mathcal{B}_{ij}^{+}\frac{|\mathbf{k}_i+\mathbf{k}_j|}{\omega_i+\omega_j}+\left(\frac{k_i\omega_i+k_j\omega_j}{\omega_i+\omega_j}\right)\left(-\frac{\mathbf{k}_i\cdot\mathbf{k}_j}{2k_ik_j}+\frac{1}{2}\right)\right\}\cos\left(\bar{\psi}_i+\bar{\psi}_j\right) \end{bmatrix} \\
& + \sum_{\substack{j_\omega=i_\omega \\ j_\theta>i_\theta}} A_i A_j \left\{\mathcal{B}_{ij}^{+}\frac{\left|\mathbf{k}_i+\mathbf{k}_j\right|}{\omega_i+\omega_j}+\left(\frac{k_i\omega_i+k_j\omega_j}{\omega_i+\omega_j}\right)\left(-\frac{\mathbf{k}_i\cdot\mathbf{k}_j}{2k_ik_j}+\frac{1}{2}\right)\right\}\cos\left(\bar{\psi}_i+\bar{\psi}_j\right)
\end{aligned}
\tag{12}
$$

We then manipulate Eq. (11) by implicitly inverting it to the expression of the reference location $\bar{\mathbf{r}}$. The assumption pertaining to the successive Eulerian orders of expansion introduces errors at the order of the mean square slope ($\int S(k)dk$, with the wave spectrum $S(k)$), which is found to be less significant than other factors in ocean surface prediction work (Grilli et al. 2011, Nouguier et al. 2013, Desmars et al. 2020). Additionally, the interaction terms in $\mathbf{r}$ are not necessarily required to be fully consistent with the second-order Eulerian description, as they are numerically unstable and associated with the higher-order Eulerian solution. In contrast, the second-order contributions in z are essential to account for the second-order nonlinear properties (Nouguier et al. 2015, Guérin et al. 2019). We thus discard the double summations except for the last term related to the Stokes drift $\mathbf{U}_{s0}$:

$$
\bar{\mathbf{r}} \approx \mathbf{r} + \sum_{i=1}^{N} A_i\frac{\mathbf{k}_i}{k_i}\sin\bar{\psi}_i - \frac{1}{2}\mathbf{U}_{s0}t
\tag{13}
$$

where a tilde denotes any quantity modified with the effect of Stokes drift, i.e. $\bar{\psi}_i=\mathbf{k}_i\cdot\mathbf{r}-\tilde{\omega}_i t-\varphi_i$ and $\tilde{\omega}_i=\omega_i+\frac{1}{2}\mathbf{k}_n\cdot\mathbf{U}_{s0}$. The Stokes drift refers to a net movement (or velocity) of a Lagrangian particle in its propagating direction:

$$
\mathbf{U}_{s0} = \sum_{i=1}^{N} {A_i}^2\mathbf{k}_i\omega_i
\tag{14}
$$

The nonlinear sea surface is provided by combining Eqs. (12) and (13). Further splitting the double summation with $j_\omega > i_\omega$ into one between non-aligned wave vectors ($j_\theta > i_\theta$) and the other between

aligned wave vectors ($j_\theta = i_\theta$), the free surface elevation provided by CICWM reads

$$\begin{aligned}\eta(\mathbf{r},t) = {} & \frac{1}{2}\sum_{i=1}^{N} {A_i}^2 k_i + \sum_{i=1}^{N} A_i \cos\Psi_i \\ & + 2\sum_{\substack{j_\omega>i_\omega \\ j_\theta>i_\theta}} A_i A_j \left[\left(\mathcal{IC}_{ij}^1 + \mathcal{IC}_{ij}^2\right)\cos\left(\Psi_i - \Psi_j\right)\right. \\ & \left. + \left(\mathcal{IC}_{ij}^3 + \mathcal{IC}_{ij}^4\right)\cos\left(\Psi_i + \Psi_j\right)\right] \\ & + \sum_{\substack{j_\omega>i_\omega \\ j_\theta=i_\theta}} A_i A_j \left(\mathcal{IC}_{ij}^1 + \mathcal{IC}_{ij}^2\right)\cos\left(\Psi_i - \Psi_j\right) \\ & + \sum_{\substack{j_\omega=i_\omega \\ j_\theta>i_\theta}} A_i A_j \left(\mathcal{IC}_{ij}^3 + \mathcal{IC}_{ij}^4\right)\cos\left(\Psi_i + \Psi_j\right)\end{aligned} \tag{15}$$

where the new interaction coefficients are

$$\begin{aligned}\mathcal{IC}_{ij}^1 &= \mathcal{B}_{ij}^- \frac{\left|\mathbf{k}_i - \mathbf{k}_j\right|}{\omega_i - \omega_j} = \frac{\omega_i\omega_j}{k_i k_j}\frac{\left|\mathbf{k}_i - \mathbf{k}_j\right|\left(\mathbf{k}_i\cdot\mathbf{k}_j + k_i k_j\right)}{\left(\omega_i - \omega_j\right)^2 - g\left|\mathbf{k}_i - \mathbf{k}_j\right|} \\ \mathcal{IC}_{ij}^2 &= \left(\frac{k_i\omega_i - k_j\omega_j}{\omega_i - \omega_j}\right)\left(\frac{\mathbf{k}_i\cdot\mathbf{k}_j}{2k_i k_j} + \frac{1}{2}\right) \\ \mathcal{IC}_{ij}^3 &= \mathcal{B}_{ij}^+ \frac{\left|\mathbf{k}_i + \mathbf{k}_j\right|}{\omega_i + \omega_j} = \frac{\omega_i\omega_j}{k_i k_j}\frac{\left|\mathbf{k}_i + \mathbf{k}_j\right|\left(\mathbf{k}_i\cdot\mathbf{k}_j - k_i k_j\right)}{\left(\omega_i + \omega_j\right)^2 - g\left|\mathbf{k}_i + \mathbf{k}_j\right|} \\ \mathcal{IC}_{ij}^4 &= \left(\frac{k_i\omega_i + k_j\omega_j}{\omega_i + \omega_j}\right)\left(-\frac{\mathbf{k}_i\cdot\mathbf{k}_j}{2k_i k_j} + \frac{1}{2}\right)\end{aligned} \tag{16}$$

and the nonlinear phase function Ψ_i includes both the effects of the nonlinear phase shift and Stokes drift:

$$\Psi_i = \mathbf{k}_i\cdot\left[\mathbf{r} + \sum_{j=1}^{N} A_j\frac{\mathbf{k}_j}{k_j}\sin\tilde{\psi}_j\right] - \tilde{\omega}_i t - \varphi_i \tag{17}$$

Using the Eulerian description, all the nonlinear models in this paper incorporate third-order effects solely as corrections to the dispersion relation in wave steepness. On the other hand, Eq. (15) shows that CICWM includes non-resonant nonlinear interactions at second-order, generating new wave components. In other words, the selection rules for resonant three-wave interactions are not generally satisfied. Tanaka (2001) demonstrated non-resonant interactions, including these three-wave interactions, do not significantly contribute to the short-term evolution of deep-water ocean spectra. We discovered that including the additional second-order components enhances the accuracy of ocean surface descriptions in directional sea states, which will be detailed in Section 5.2.

Introducing the wave parameters represented by a combination of A_i and φ_i:

$$(a_n, b_n) = (A_n\cos\varphi_n, A_n\sin\varphi_n) \tag{18}$$

and redefining the nonlinear phase function with the unit wave vector $\hat{\mathbf{k}}_i = \frac{\mathbf{k}_i}{k_i}$:

$$\Psi_n = \mathbf{k}_n\cdot[\mathbf{r} - \sum_{i=1}^{N}\hat{\mathbf{k}}_i(-a_i\sin\tilde{\psi}_i + b_i\cos\tilde{\psi}_i)] - \tilde{\omega}_n t \tag{19}$$

and $\tilde{\psi}_i = \mathbf{k}_i\cdot\mathbf{r} - \tilde{\omega}_i t$ with $\mathbf{U}_{s0} = \sum_{i=1}^{N}({a_i}^2 + {b_i}^2)\omega_i\mathbf{k}_i$.

With further manipulations, the final free surface elevation form of CICWM in the case of multidirectional waves (or short-crested waves) becomes

$$\begin{aligned}\eta(\mathbf{r},t) = {} & \sum_{i=1}^{N}\left[a_i\cos\Psi_i + b_i\sin\Psi_i + \frac{1}{2}({a_i}^2 + {b_i}^2)k_i\right] \\ & + \sum_{\substack{j_\omega\geq i_\omega \\ j_\theta\geq i_\theta}}\begin{bmatrix}\mathcal{CIC}_{ij}^1\left(a_j\cos\Psi_j + b_j\sin\Psi_j\right)\left(a_i\cos\Psi_i + b_i\sin\Psi_i\right) \\ +\mathcal{CIC}_{ij}^2\left(a_j\sin\Psi_j - b_j\cos\Psi_j\right)\left(a_i\sin\Psi_i - b_i\cos\Psi_i\right)\end{bmatrix}\end{aligned} \tag{20}$$

where the combinations of interaction coefficients are

$$\mathcal{CIC}_{ij}^1 = \begin{cases}2\mathcal{IC}_{ij}^1 + 2\mathcal{IC}_{ij}^2 + 2\mathcal{IC}_{ij}^3 + 2\mathcal{IC}_{ij}^4, & \text{if } j_\omega > i_\omega \text{ and } j_\theta > i_\theta \\ \mathcal{IC}_{ij}^1 + \mathcal{IC}_{ij}^2, & \text{if } j_\omega > i_\omega \text{ and } j_\theta = i_\theta \\ \mathcal{IC}_{ij}^3 + \mathcal{IC}_{ij}^4, & \text{if } j_\omega = i_\omega \text{ and } j_\theta > i_\theta \\ 0, & \text{if } j_\omega = i_\omega \text{ and } j_\theta = i_\theta\end{cases} \tag{21}$$

$$\mathcal{CIC}_{ij}^2 = \begin{cases}2\mathcal{IC}_{ij}^1 + 2\mathcal{IC}_{ij}^2 - 2\mathcal{IC}_{ij}^3 - 2\mathcal{IC}_{ij}^4, & \text{if } j_\omega > i_\omega \text{ and } j_\theta > i_\theta \\ \mathcal{IC}_{ij}^1 + \mathcal{IC}_{ij}^2, & \text{if } j_\omega > i_\omega \text{ and } j_\theta = i_\theta \\ -\mathcal{IC}_{ij}^3 - \mathcal{IC}_{ij}^4, & \text{if } j_\omega = i_\omega \text{ and } j_\theta > i_\theta \\ 0, & \text{if } j_\omega = i_\omega \text{ and } j_\theta = i_\theta\end{cases} \tag{22}$$

3. Methods

The algorithms for real-time phase-resolved ocean wave forecasting vary depending on the wave model, as the development of data assimilation methods for reconstructing waves from wave observations is model-based. Wave propagation is achieved by forward propagating in space and time, relying on initial wave conditions optimized during the wave reconstruction step.

3.1. Wave models

To investigate the impacts of newly added nonlinear summations in CICWM, it is imperative to compare CICWM and ICWM using experimental data in both multidirectional and unidirectional wave fields. Previous studies on real-time wave prediction (Desmars et al. 2020, Kim et al. 2023a, Desmars et al. 2023) considered ICWM as the most mature model, alongside two additional wave models: the linear wave theory model (LWT) and the linear wave theory model modified with a corrected dispersion relationship (LWT-CDR). There exists potential for the development of an intermediate model between LWT-CDR and ICWM. Further exploration into the nonlinear phase shift might lead to the simplification of ICWM, similar to the manner in which nonlinear terms are discarded in the derivation of ICWM. This simplified version of ICWM, termed Simplified ICWM (SICWM), retains more nonlinear terms than LWT-CDR, while maintaining the same phase function in both models. This section provides a comprehensive overview of the five wave models used in this study, ordered in terms of development regarding nonlinear aspects, from LWT to CICWM.

3.1.1. LWT

The traditional method based on linear wave theory (LWT) provides the most basic formulation of free surface elevation:

$$\begin{aligned}\eta^{\mathrm{LWT}}(x,y,t) &= \sum_{i_\theta=1}^{N_\theta}\sum_{i_\omega=1}^{N_\omega}\left[a_{(i_\omega,i_\theta)}\cos\psi_{(i_\omega,i_\theta)} + b_{(i_\omega,i_\theta)}\sin\psi_{(i_\omega,i_\theta)}\right] \\ &= \sum_{i=1}^{N}\left[a_i\cos\psi_i + b_i\sin\psi_i\right]\end{aligned} \tag{23}$$

where the linear phase function $\psi_i = \mathbf{k}_i\cdot\mathbf{r} - \omega_i t$ is redefined without the random phase.

3.1.2. LWT-CDR

In the development sequence, the second model is based on linear wave theory with a corrected dispersion relationship (LWT-CDR). By comparing LWT and LWT-CDR, one can quantify the effect of Stokes drift on the resulting ocean wave surfaces. The free surface elevation by LWT-CDR is given by

$$\begin{aligned}\eta^{\text{LWT-CDR}}(x,y,t) &= \sum_{i_\theta=1}^{N_\theta}\sum_{i_\omega=1}^{N_\omega}\left[a_{(i_\omega,i_\theta)}\cos\tilde{\psi}_{(i_\omega,i_\theta)} + b_{(i_\omega,i_\theta)}\sin\tilde{\psi}_{(i_\omega,i_\theta)}\right] \\ &= \sum_{i=1}^{N}\left[a_i\cos\tilde{\psi}_i + b_i\sin\tilde{\psi}_i\right]\end{aligned} \tag{24}$$

where the modified phase function is also redefined as $\tilde{\psi}_i = \mathbf{k}_i\cdot\mathbf{r} - \tilde{\omega}_i t$.

3.1.3. SICWM

In comparison to the modified phase function $\tilde{\psi}_i$, the nonlinear phase function Ψ_i in Eq. (19) involves the nonlinear phase shift, i.e. summation in Eq. (19). Performing a Taylor expansion of η^{ICWM} around $\tilde{\psi}_i$, the influence of a nonlinear property in the nonlinear phase (i.e., bound waves) can be formulated as nonlinear wave-wave interaction terms. We can then discard the nonlinear terms pertaining to different wave components. Consequently, the simplified ICWM (SICWM) is derived by incorporating additional trigonometric functions featuring a double phase $2\tilde{\psi}_i$ into LWT-CDR:

$$\begin{aligned}\eta^{\mathrm{SICWM}}(x,y,t) = &\sum_{i=1}^{N}[a_i\cos\tilde{\psi}_i + b_i\sin\tilde{\psi}_i] \\ &+ \frac{1}{2}\sum_{i=1}^{N}[({a_i}^2 - {b_i}^2)k_i\cos 2\tilde{\psi}_i + 2a_ib_ik_i\sin 2\tilde{\psi}_i]\end{aligned} \tag{25}$$

The full derivation of SICWM is provided in Appendix A. As a reminder, we here use the index vector i with single summations to avoid the complexity of second-order terms in double summations with i_ω and i_θ.

3.1.4. ICWM

The numerically efficient model proposed in Guérin et al. (2019), ICWM, fully incorporates the effect of the nonlinear phase shift via the nonlinear phase function Ψ_i, as opposed to SICWM. The explicit form of surface elevation is provided by ICWM:

$$\eta^{\mathrm{ICWM}}(x,y,t) = \sum_{i=1}^{N}[a_i\cos\Psi_i + b_i\sin\Psi_i + \frac{1}{2}({a_i}^2 + {b_i}^2)k_i] \tag{26}$$

where Ψ_i is the redefined nonlinear phase function in Eq. (19).

3.1.5. CICWM

The last and the most mature tool, with more nonlinear effects including second-order Lagrangian interaction terms, is CICWM. Eq. (20) can be rewritten as a more detailed form with consideration of Eqs. (21) and (22):

$$\begin{aligned}\eta^{\mathrm{CICWM}}(x,y,t) = &\sum_{i=1}^{N}[a_i\cos\Psi_i + b_i\sin\Psi_i + \frac{1}{2}({a_i}^2 + {b_i}^2)k_i] \\ &+ \sum_{\substack{j_\omega>i_\omega \\ j_\theta>i_\theta}}\begin{bmatrix} CIC_{ij}^1\left(a_j\cos\Psi_j + b_j\sin\Psi_j\right)\left(a_i\cos\Psi_i + b_i\sin\Psi_i\right) \\ +CIC_{ij}^2\left(a_j\sin\Psi_j - b_j\cos\Psi_j\right)\left(a_i\sin\Psi_i - b_i\cos\Psi_i\right)\end{bmatrix} \\ &+ \sum_{\substack{j_\omega>i_\omega \\ j_\theta=i_\theta}}\begin{bmatrix} CIC_{ij}^1\left(a_j\cos\Psi_j + b_j\sin\Psi_j\right)\left(a_i\cos\Psi_i + b_i\sin\Psi_i\right) \\ +CIC_{ij}^2\left(a_j\sin\Psi_j - b_j\cos\Psi_j\right)\left(a_i\sin\Psi_i - b_i\cos\Psi_i\right)\end{bmatrix} \\ &+ \sum_{\substack{j_\omega=i_\omega \\ j_\theta>i_\theta}}\begin{bmatrix} CIC_{ij}^1\left(a_j\cos\Psi_j + b_j\sin\Psi_j\right)\left(a_i\cos\Psi_i + b_i\sin\Psi_i\right) \\ +CIC_{ij}^2\left(a_j\sin\Psi_j - b_j\cos\Psi_j\right)\left(a_i\sin\Psi_i - b_i\cos\Psi_i\right)\end{bmatrix}\end{aligned} \tag{27}$$

where the first summation corresponds to the surface elevation of ICWM. Hence, terms involving CIC_{ij}^1 and CIC_{ij}^2 account for amplitude and phase modulations to ICWM, respectively. It is noteworthy that the second double summation with $j_\theta = i_\theta$ represents the second-order interaction terms that are valid for both long-crested waves and short-crested waves, and Guérin et al. (2019) examined these terms via a synthetic reference dataset. On the other hand, the first and third double summations are additional terms for short-crested waves only.

3.2. Data assimilation

Given that the wave parameters, represented by a_n and b_n, across the wave fields of interest remain constant in both time and space, we can use model-based inversion approaches to deduce the optimal parameters from ocean surface measurements $\bar{\eta}$. By means of variational assimilation (Blondel et al., 2010), spatio-temporal observations are leveraged to minimize a quadratic cost function that evaluates the disparity between observed ($\bar{\eta}_l$) and computed (η_l) wave surface elevations:

$$F(\mathbf{p}) = \frac{1}{2}\sum_{l=1}^{L}[\eta_l(\mathbf{p}) - \bar{\eta}_l]^2 = \frac{1}{2}\sum_{j=1}^{J}\sum_{k=1}^{K}[\eta_{(j,k)}(\mathbf{p}) - \bar{\eta}_{(j,k)}]^2 \tag{28}$$

where $\mathbf{p} = [a_1,\ldots,a_N,b_1,\ldots,b_N]^T$ is the vector of amplitude parameters to be optimized. The subscript l denotes each spatio-temporal measurement point, defined as $l = (j,k)$ representing both spatial and temporal dimensions. The total number of spatio-temporal data points L is a multiplication of the numbers of spatial data (J) and temporal data (K), namely, $L = J \times K$.

In order to optimize the amplitude parameters, taking the derivatives of the cost function with respect to a_n and b_n leads to the system of equations with matrix operation $\mathbf{Ap} = \mathbf{B}$. The coefficient matrix $\mathbf{A}$ is a $2N \times 2N$ matrix composed of $A_{(m,n)}$, $A_{(m,N+n)}$, $A_{(N+m,n)}$, and $A_{(N+m,N+n)}$, with $(n,m) \in \{1,\ldots,N\}^2$. On the other hand, the observation vector $\mathbf{B}$ contains $2N$ components (i.e., B_m and B_{N+m}). To tackle the ill-posed assimilation challenge arising from practical constraints, such as uneven sampling by optical sensors, Tikhonov regularization is utilized, but not explained for brevity.

First, the linear assimilation method is obtained by using

$$\begin{aligned}A_{(m,n)}^{LWT} &= \sum_{l=1}^{L}\cos\psi_{nl}P_{ml}^{LWT} \\ A_{(m,N+n)}^{LWT} &= \sum_{l=1}^{L}\sin\psi_{nl}P_{ml}^{LWT} \\ A_{(N+m,n)}^{LWT} &= \sum_{l=1}^{L}\cos\psi_{nl}Q_{ml}^{LWT} \\ A_{(N+m,N+n)}^{LWT} &= \sum_{l=1}^{L}\sin\psi_{nl}Q_{ml}^{LWT}\end{aligned} \tag{29}$$

and

$$\begin{aligned}B_m^{LWT} &= \sum_{l=1}^{L}\bar{\eta}_l P_{ml}^{LWT} \\ B_{N+m}^{LWT} &= \sum_{l=1}^{L}\bar{\eta}_l Q_{ml}^{LWT}\end{aligned} \tag{30}$$

with

$$\begin{aligned}P_{ml}^{LWT} &= \cos\psi_{ml} \\ Q_{ml}^{LWT} &= \sin\psi_{ml}\end{aligned} \tag{31}$$

where $(n,m) \in \{1,\ldots,N\}^2$, $l = 1$ to L, and $\psi_{ml} = \mathbf{k}_{ml}\cdot\mathbf{r}_l - \omega_m t_l$.

All the wave models in this study, except for LWT, require iterative processing in the data assimilation phase, as both matrices $\mathbf{A}$ and $\mathbf{B}$ contain solutions of matrix operations (i.e., a_n and b_n). Given the considerably challenging computational complexity for real-time predictions, particularly in directional sea states, Kim et al. (2023a) proposed a simplified nonlinear assimilation method by modifying matrices $\mathbf{A}$ and $\mathbf{B}$ for nonlinear wave models. In their study, it was observed that for their particular application, even the most basic nonlinear model (i.e., LWT-CDR) cannot achieve real-time wave forecasting in directional wave cases without employing this simplification. Hence, the data assimilation methods for all the nonlinear models in this study have been developed based on this simplification. For example, the

Table 1
Directional information of experimental data and numerical simulations.

Case	s	J_θ	θ_{lim} (°)	N_θ
A	15	11	35	5
B	25	9	35	5
C	60	7	25	3
D	∞	1	0	1

formulations for LWT-CDR are given by:

$$\begin{aligned} A^{LWT-CDR}_{(m,n)} &= \sum_{l=1}^{L} \cos\tilde{\psi}_{nl} P^{LWT}_{ml} \\ A^{LWT-CDR}_{(m,N+n)} &= \sum_{l=1}^{L} \sin\tilde{\psi}_{nl} P^{LWT}_{ml} \\ A^{LWT-CDR}_{(N+m,n)} &= \sum_{l=1}^{L} \cos\tilde{\psi}_{nl} Q^{LWT}_{ml} \\ A^{LWT-CDR}_{(N+m,N+n)} &= \sum_{l=1}^{L} \sin\tilde{\psi}_{nl} Q^{LWT}_{ml} \end{aligned} \tag{32}$$

where $\tilde{\psi}_{il} = \mathbf{k}_i \cdot \mathbf{r}_l - \tilde{\omega}_i t_l$. For a comprehensive yet compact presentation, the formulations (i.e., **A** and **B**) for the remaining models and details in the iterative process are provided in Appendix B.

4. Experimental data

The present work received support from the European H2020 FLOATECH project. During one of the FLOATECH project campaigns, experimental observations were collected at École Centrale de Nantes (ECN) (Bonnefoy et al., 2023). The ocean engineering tank is 30 m wide, 50 m long, and 5 m deep, featuring a wavemaker at one end, composed of 48 individual hinged flaps, and a 7-m long passive stainless steel beach at the opposite end. The experiments in the wave tank were carried out under irregular sea states, employing a Pierson–Moskowitz spectrum (Pierson and Moskowitz, 1964) with a peak period $T_p = 12$ s at full scale and scaled geometrically to 1:40 (also scaled to 1: $\sqrt{40}$ in time based on the Froude scaling law).

The main purpose of the wave tests is to verify numerical wave models for ocean wave prediction at our designated location. We considered directional sea states with several directional spreads, along with a unidirectional case D (see Fig. 1 and Table 1). The angular spreading function used to define directional spreads in the wave field for this study was outlined in Mitsuyasu et al. (1975):

$$G(\theta) = \frac{2^{2s-1}}{180}\frac{(s!)^2}{(2s)!}\cos^{2s}\left(\frac{\theta}{2}\right) \quad \text{for } \theta \in [-180°, 180°] \tag{33}$$

where θ denotes the propagating direction with 0° the average direction of propagation, and s refers to the directional spreading factor.

Herein, we restrict our attention to moderate nonlinear waves characterized by a wave steepness $H_s/L_p = 3.1\%$ in deep water, with a significant wave height $H_s = 7$ m and a peak wavelength $L_p = 225$ m at full scale. The relative water depth is $k_p d \approx 5.6$, where k_p is the peak wavenumber and d is the water depth. Additional results and analysis involving varying values of wave steepness can be found in Desmars et al. (2020) and Kim et al. (2024b), using an equivalent experimental setup. The differences between the results simulated by the models were not relatively pronounced, mainly due to experimental noise and the presence of wave-breaking in cases with weaker nonlinearity (e.g., $H_s/L_p = 2.2\%$) and stronger nonlinearity (e.g., $H_s/L_p = 4.1\%$), respectively. Comparison with CICWM exhibited a similar tendency; hence, the results are not presented here.

To simulate a scenario involving a structure-mounted optical system, a matrix of $J_r \times J_\theta$ rays in the xy-plane was created by leveraging a straight rotating structure with 20 wave gauges, denoted as $J_r = 20$ (see Fig. 2). Here, J_θ denotes the number of directional arrays used for the measurement. Cases with greater directional spreading involved considering a wider range of angular positions for the wave gauges, with increased values of J_θ. Table 1 summarizes directional information of experimental data and numerical simulations. The process of optimizing the directional limit θ_{lim}, along with the number of directional components N_θ, will be described later in this paper.

Here, the spatial distribution mimics the typical uneven sampling based on LIDAR cameras, but it could also be reconstructed for cases using X-band radars. The wave surface was observed at four additional downstream wave gauges: WG21, WG22, WG23, and WG24, located at distances of approximately $0.15L_p$, $0.21L_p$, $0.24L_p$, and $0.28L_p$ from the observation zone, respectively, with WG21 corresponding to our target point. We presumed that all wave components from the wavemaker had propagated throughout the entire experimental domain by $t_a/T_p \approx 158$. Furthermore, we used the time series until the completion of the experimental measurements, where $t_b/T_p \approx 664$ and $t_b - t_a \approx 506T_p$, as the wave surface elevation was collected until the wavemaker was turned off. Due to this long experimental duration, reflections at the absorbing beach were confirmed in the wave basin. The reflection rate ranged between 5% and 10% for the cases considered in this study. Additionally, the experimental noise resulting from wave reflections, along with other uncertainties such as wave gauge calibration and small gaps between each wave paddle, was quantified to be a maximum of 7% of the target significant wave height (Bonnefoy et al., 2023). Further detailed information about the experimental setup, including a sketch of the optical system, can be found in Kim et al. (2023a) and Bonnefoy et al. (2023).

Lastly, most phase-resolved reconstruction attempts consider wave shadowing as a dominant source of error in actual sea-going applications. Wave shadowing occurs when areas behind a gravity wave are not directly measured by the LIDAR camera or X-band radar, leading to gaps in the spatial sampling of the free surface elevation. For X-band radars, shadowing effects can be mitigated by using a shadowing mask during the inversion process. In addition to the highly non-uniform spatial gaps, the relatively sparse and aperiodic temporal observations require post-processing techniques, such as the remapping method (Belmont et al., 2007). Furthermore, a new technique called conflation has recently been introduced, which combines multiple RADAR scan datasets to create a multi-segment dataset along with a corresponding theoretical model (Belmont, 2023). In this experiment, however, wave-shadowing effects were not reproduced; the actual variations in probe location, which would result from the intersection of an optical ray with an irregular, evolving free surface, were not considered. Future work will focus on incorporating noise and shadowing into wave data to develop more realistic algorithms, even if this introduces additional numerical complexity (Simpson et al., 2020).

5. Numerical simulations

This section evaluates the performance of wave models and analyzes discrepancies among them, with a particular emphasis on short-term wave prediction relevant to feed-forward wave-based control systems for floating offshore wind turbines (Guo et al. 2017, Al et al. 2020, Kim et al. 2024b). Following prior literature (Naaijen et al. 2014, Desmars et al. 2020, Kim et al. 2023a among others), our assessment primarily relies on the normalized misfit indicator over partially overlapping surface samples:

$$\varepsilon(x,y,t) = \frac{1}{N_s}\sum_{i=1}^{N_s}\frac{\left|\eta_{pred,i}(x,y,t) - \eta_{ref,i}(x,y,t)\right|}{H_s} \tag{34}$$

where $\eta_{pred,i}$ and $\eta_{ref,i}$ represent the prediction and reference surface elevation of the ith sample, respectively. Here, N_s is the number of surface samples required for prediction error convergence, and H_s is the significant wave height of the reference surface elevation. Analyzing the averaged prediction error of CICWM with increasing N_s, we

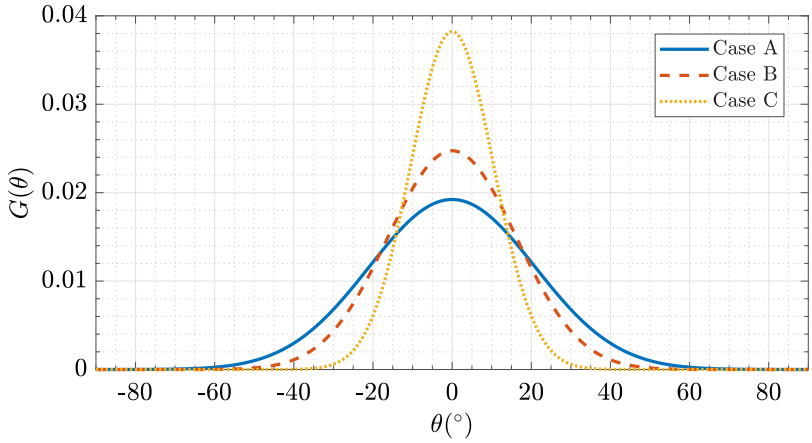

Fig. 1. Directional spreading for multidirectional cases (——: Case A; – – –: Case B; ·····: Case C).

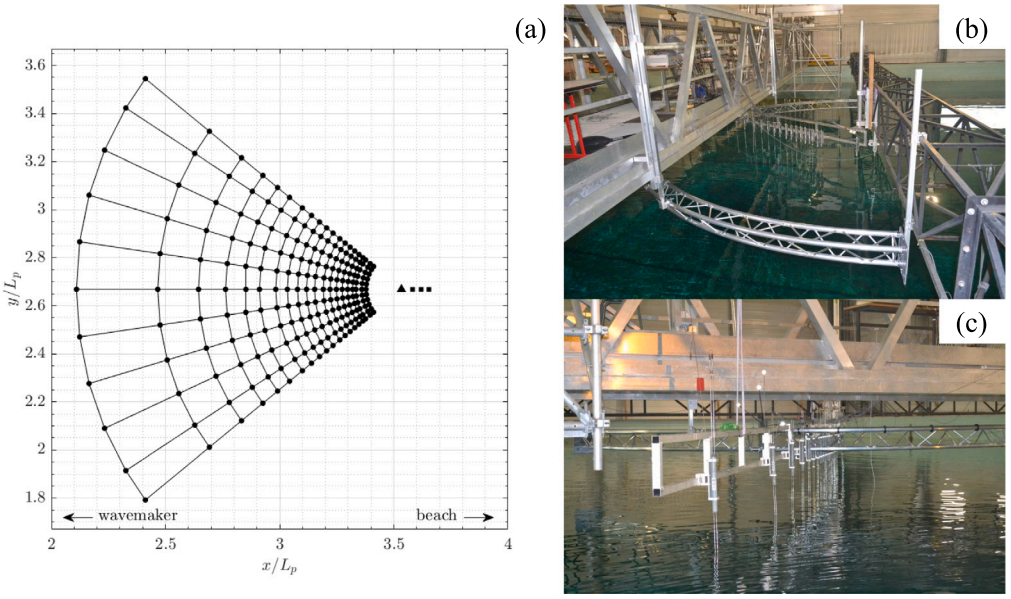

Fig. 2. (a) Location of wave gauges; (b, c) wave gauges mounted on rotating structure (•: wave observations; ▲: location of turbine, WG21; ■ : three additional downstream WG22, WG23, and WG24).

justified using the same condition as in Kim et al. (2023a) (i.e., $N_s = 400$). Additionally, we chose the time step in wave observation data $\Delta t/T_p = 0.053$ as the shifting time between the consecutive samples, as it was found to be effective.

When working with limited spatio-temporal wave data, accurate phase-resolved wave prediction is confined to the spatio-temporal prediction zone. Following the methodology outlined in Kim et al. (2024a), the prediction zone in time is bounded by $t_{\min}$ and $t_{\max}$. The normalized misfit error is then temporally averaged over the prediction zone $t \in [t_{\min}, t_{\max}]$ to quantify the synoptic accuracy of the wave forecast:

$$\varepsilon^p(x,y) = \frac{1}{t_{\max} - t_{\min}} \int_{t_{\min}}^{t_{\max}} \varepsilon(x,y,t)\, dt \tag{35}$$

In both unidirectional and directional sea states, wave fields were generated with a single phase set for each case. However, we ensured the generalizability of results by synthesizing surface samples from each sea state over a sufficiently long time. Due to the variability between realizations (i.e., surface samples), it is necessary to determine the optimal value of N_s (or T_c) that results in the convergence of the misfit indicator between the surface predicted by CICWM and the reference surface. Fig. 3 shows the averaged prediction error of CICWM with increasing T_c/T_p. It is justified to use the same condition as in Kim et al. (2023a) for ICWM (i.e., $T_c/T_p \approx 25$ or $N_s = 400$). In this optimizing task, the wave parameters, including the numbers of wave parameters N_ω and N_θ, as well as the assimilation time T_a, need to be prespecified. The process of finding these values will be explained in the following section.

5.1. Model parameters

To provide accurate and expedited wave forecasting from spatio-temporal data acquired by an optical sensor, it is important to determine the relevant assimilation time T_a, or the number of measurement points in time K. Fig. 4 shows that the assimilation time resulting in convergence error for CICWM is $T_a/T_p \approx 5.2$ (or $K = 100$).

Kim et al. (2024a) achieved real-time wave prediction by using a direction range of $[\theta_{\min}, \theta_{\max}] = [-\theta_{\lim}, \theta_{\lim}]$, with the directional limit $\theta_{\lim}$ and the number of directional components N_θ suitable for each directional case. Panels (a), (b), and (c) of Fig. 5 illustrate the optimizing process of numerical setups in the directional domain, as summarized in Table 1. Considering the actual spatial range of wave observations (Desmars et al., 2020) and the relationship for the last

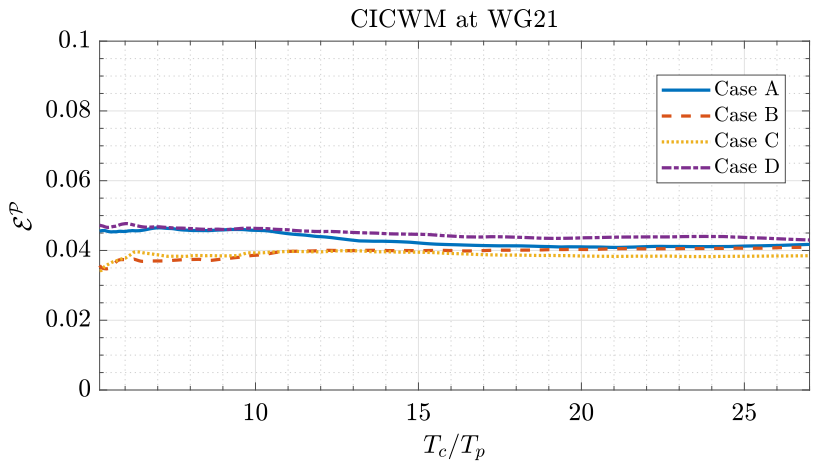

Fig. 3. Prediction error of CICWM at WG21 against T_c/T_p (——: Case A; – – –: Case B; ·····: Case C; —·—: Case D).

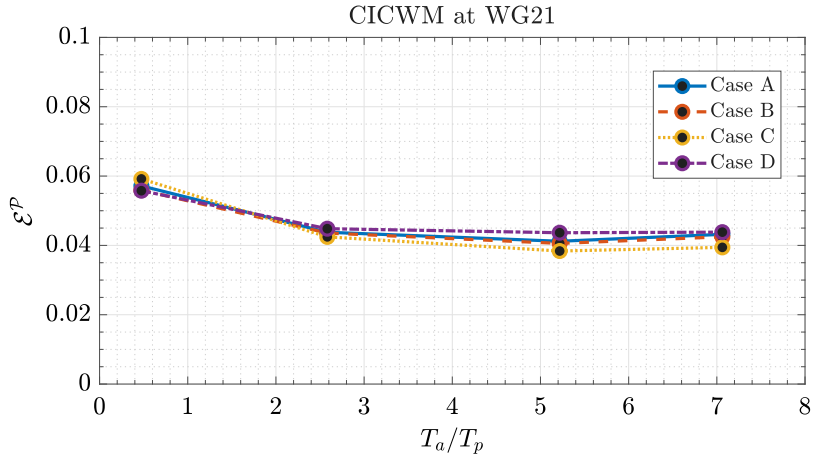

Fig. 4. Prediction error of CICWM at WG21 against T_a/T_p (——: Case A; – – –: Case B; ·····: Case C; —·—: Case D).

frequency component k_{N_ω} ($k_{N_\omega} = \frac{2N_\omega}{5}k_p$; Kim et al. 2023b), the first frequency component k_1 can be obtained. Fig. 5(d) shows that $N_\omega = 30$, where $k_{N_\omega} = 12k_p$, is the optimal choice (where N_ω is the number of frequency components). Note that the optimal numerical wave fields were found to be the same as those for ICWM in Kim et al. (2024a).

5.2. Comparison between wave models and experimental data

Before discussing the models' ability to simulate the propagation of wave fields, it is imperative to ensure that the real-time constraint is met by each model. Table 2 provides a summary of the resulting numerical efficiency (total calculation time T_{total}) and stability (iteration number and convergence probability) for the most challenging case A among the cases in this study, which involves the greatest numbers of wave data and components. The computations were performed on an Intel(R) Core(TM) i7-8700 CPU 3.20 GHz. The practical prediction zone can be obtained as $\mathfrak{T} = 21.6$ s for Case A (Kim et al., 2024a), and it was confirmed that the computation time T_{total} is sufficiently small for all the models. More details on real-time constraints under various scenarios can be found in Kim et al. (2024a). Despite its simpler nature compared to ICWM, SICWM exhibits slightly lower numerical efficiency, indicating that the presence of nonlinear terms with a double phase would be enough to offset any beneficial effects of the reduced complexity of the nonlinear phase.

According to previous studies (Desmars et al. 2020, Kim et al. 2023a), although there is an excellent overall agreement between the observed ocean surfaces and those predicted by all the models at the point of interest (WG21), the differences between the numerical wave models, including those between LWT and ICWM, do not seem visually significant. Similarly, Fig. 6 demonstrates that the additional nonlinear aspects of CICWM compared to ICWM are not visually apparent either. However, a thorough investigation of the nonlinear effects during wave propagation will be presented next, utilizing various metrics, which include not only the prediction error ratio but also the estimation of surface shape and cross-correlation.

Table 2
Comparison of numerical cost and stability for Case A where $\mathfrak{T} = 21.6$ s at full scale.

Case A	CICWM	ICWM	SICWM	LWT-CDR	LWT
T_{total} (s)	3.0	1.0	1.7	0.7	0.4
Iteration number	3.3	3.1	2.9	2.9	–
Convergence probability	93.8%	97.3%	99.5%	99.8%	–

Fig. 7 presents the prediction misfit errors ε^p of CICWM and the error ratios of CICWM compared to the other wave models for all cases at the target point. As indicated by the solid lines, CICWM demonstrates slightly better predictive accuracy for directional waves compared to that of ICWM as well as its own performance for unidirectional waves. Somewhat surprisingly, the dashed and dotted lines coincide exactly, suggesting that, for the sea states examined in this study, the differences in the nonlinear aspects between SICWM and LWT-CDR do not affect phase-resolved ocean wave forecasting. While the impact of Stokes drift, absent only in LWT, is significant only in unidirectional

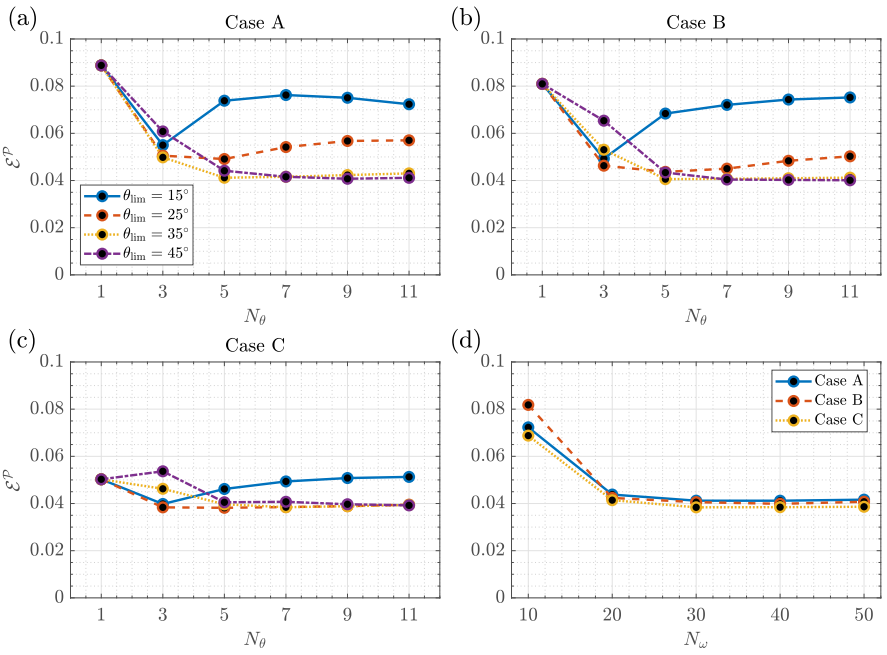

Fig. 5. (a, b, c) Prediction error of CICWM at WG21 against N_θ and $\theta_{\lim}$: (a) Case A; (b) Case B; (c) Case C (——: $\theta_{\lim} = 15°$; – – ·: $\theta_{\lim} = 25°$; ·····: $\theta_{\lim} = 35°$; —·—: $\theta_{\lim} = 45°$); (d) Prediction error of CICWM at WG21 against N_ω (——: Case A; – – ·: Case B; ·····: Case C).

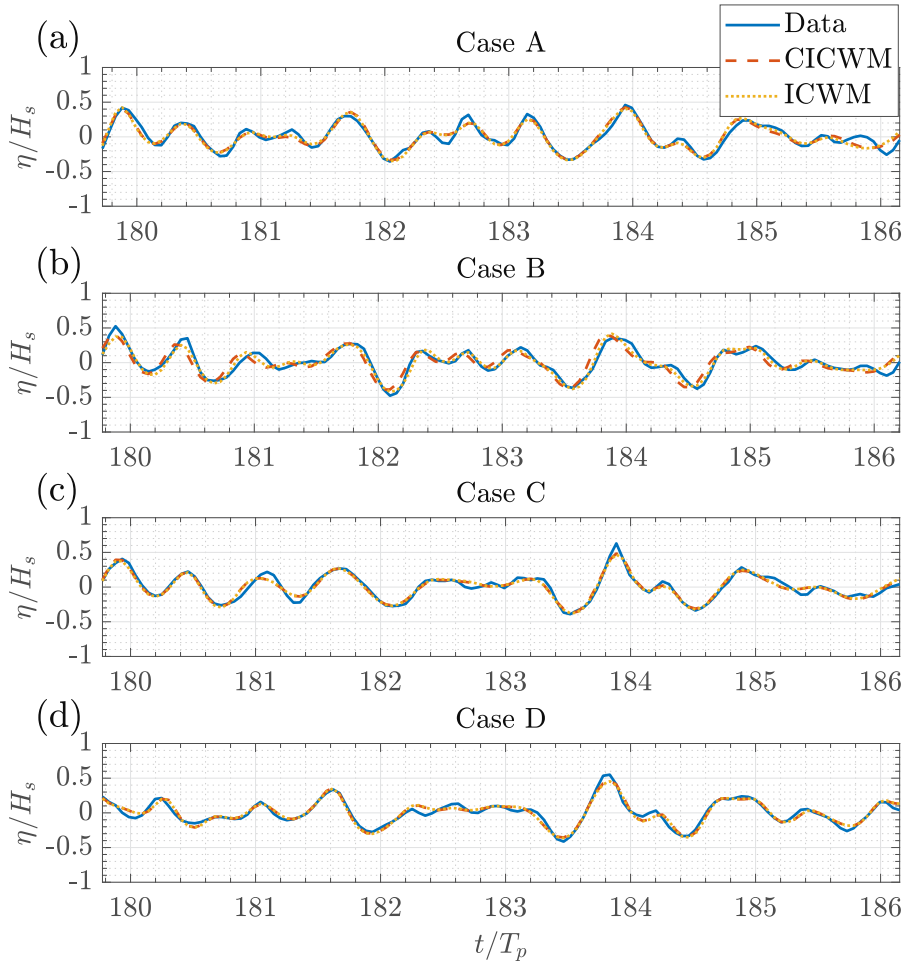

Fig. 6. Time series of surface elevation at WG21: (a) Case A; (b) Case B; (c) Case C; (d) Case D (——: Data; – – ·: CICWM; ·····: ICWM).

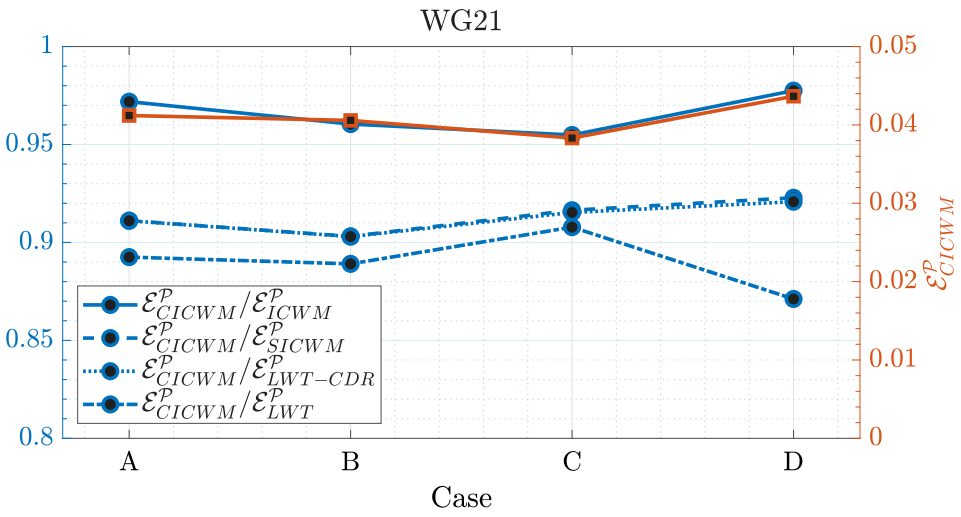

Fig. 7. Prediction error ratio (•) and prediction error of CICWM (■) at WG21 (——: CICWM to ICWM; – – –: CICWM to SICWM; ·····: CICWM to LWT-CDR; —·—: CICWM to LWT).

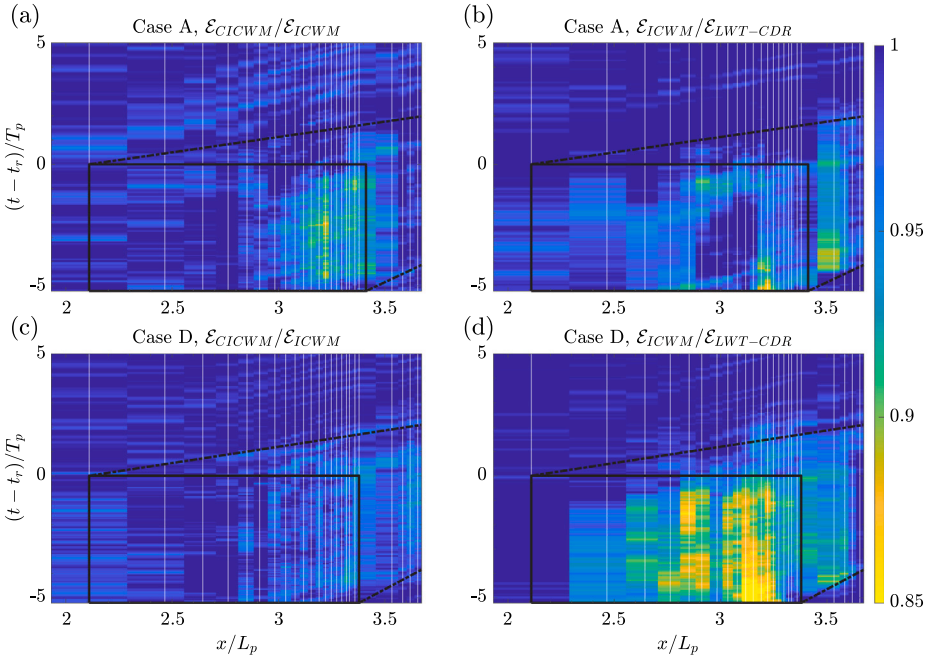

Fig. 8. Spatio-temporal evolution of prediction error ratio at all WGs along centerline where $t = t_r$ is the latest time of wave reconstruction: (a) CICWM to ICWM for Case A; (b) ICWM to LWT-CDR for Case A; (c) CICWM to ICWM for Case D; (d) ICWM to LWT-CDR for Case D (—·—: boundaries of prediction zone; vertical white lines: x-location of WGs along centerline at $y = y_c$; black rectangle: assimilated data set).

waves, comparing ICWM and LWT-CDR demonstrates that the effect of the nonlinear phase shift remains consistently significant in both directional and unidirectional cases (Kim et al., 2023a).

For a more detailed examination of the nonlinear second-order interaction terms in CICWM for both short- and long-crested waves, Fig. 8 provides the spatio-temporal evolution of the prediction error ratio in the directional case A (panels a and b) and the unidirectional case D (panels c and d), respectively. The ratio of accuracy between models appears to vary across different time steps. By calculating the coefficients of variance (COV) of the error ratio over the prediction zone in time, we found that the COV value does not exceed approximately 4% at any of the downstream wave gauges, thanks to the use of a sufficient number of surface samples N_s. As concluded in Guérin et al. (2019), the nonlinear interactions exhibit relatively minor effects on the evolution of surface waves in Case D, as shown in Fig. 8(c). Conversely, in Case A, their impact is relatively significant and comparable to that of the nonlinear phase shift, which is the discrepancy between ICWM and LWT-CDR. This outcome is not surprising due to the added interactions present in multidirectional sea states, such as the first and third double summations on the right-hand side of Eq. (27).

Fig. 8 shows that the enhancements from incorporating nonlinear effects become less pronounced as the waves propagate in space at the downstream wave gauges. This indicates that the improvements from the additional nonlinear terms in both CICWM and ICWM are primarily concentrated on the reconstructed part of the wave field, while the effect of Stokes drift in LWT-CDR remains relatively pronounced with

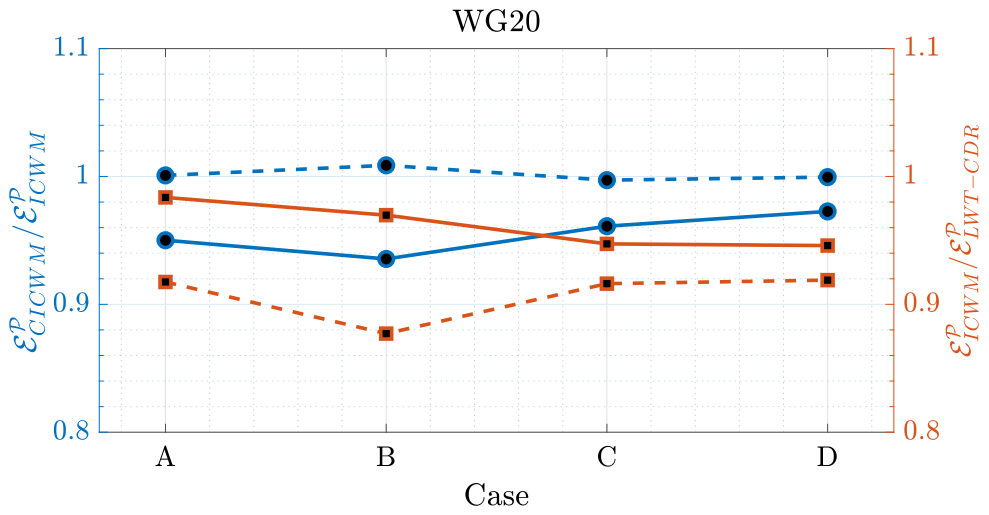

Fig. 9. Comparison of prediction error between CICWM and ICWM (•); ICWM and LWT-CDR (■) at WG20 (——: surface elevation η; – – ·: surface slope ss).

propagating in space from the observation zone (Desmars et al., 2020). Furthermore, the wave components in frequency and direction, reconstructed based on the observation zone, become increasingly limited in their ability to explain the physical representation of the wave field with increasing distance from the observation zone (Kim et al., 2023a).

Additionally, predicting the free surface slope is essential for remote sensing applications, particularly in severe sea conditions where wave behavior becomes nonlinear (Nouguier et al. 2010, 2013). The close proximity of the last two observation gauges along the centerline (referred to as WG19 and WG20), with a distance of approximately $0.02L_p$, ensures the computation of an estimation of the surface slope:

$$ss(t) = \frac{\eta(x_{20}, y_c, t) - \eta(x_{19}, y_c, t)}{x_{20} - x_{19}} \tag{36}$$

where x_{19} and x_{20} respectively represent the x-coordinates of WG19 and WG20. To further study forecasting of the sea surface shape rather than the sea surface elevation (Taylor, 2001), we normalize the prediction and reference surface elevations by their own standard deviations (i.e., $\hat{\eta}_{pred} = \eta_{pred}/\sigma_{\eta_{pred}}$ and $\hat{\eta}_{ref} = \eta_{ref}/\sigma_{\eta_{ref}}$) and obtain the maximum cross-correlation $\max(C)$ and corresponding time-lag $\arg\max(C)$:

$$C(\tau) = \frac{1}{t_{\max} - t_{\min}} \int_{t_{\min}}^{t_{\max}} \hat{\eta}_{pred}(t) \times \hat{\eta}_{ref}(t+\tau) dt \tag{37}$$

where 1 and 0 correspond to the ideal model for $\max(C)$ and $\arg\max(C)$, respectively.

In Fig. 9, the improvement by CICWM over ICWM in describing the free surface elevation at the last observation gauge is either greater or similar to that by ICWM over LWT-CDR for the directional cases. However, it is evident that the surface slope description is only enhanced by the nonlinear phase shift in ICWM regardless of whether the wave field is directionally spread or not, which is consistent with the results in Fig. 10. It should be noted that the high-frequency spectra are also almost identically estimated by both CICWM and ICWM (not shown here for conciseness). Therefore, one can conclude that while the nonlinear phase function of ICWM contributes to the description of both surface elevation and shape, the second-order nonlinear interactions of CICWM only impact the elevation.

6. Conclusions

Guérin et al. (2019) introduced the Improved Choppy Wave Model (ICWM), a robust and straightforward model aimed at achieving a second-order Lagrangian expansion of surface waves. Their study demonstrated that the second-order Lagrangian nonlinear interaction terms are non-negligible only over a short period, leading to their exclusion from the development of ICWM. However, these terms in directional wave fields were left unexplored for future research. Additionally, while Kim et al. (2023a) successfully implemented ICWM for real-time ocean wave prediction over a short time horizon within the feed-forward wave-based control system for floating offshore wind turbines, the accuracy of wave predictions needs further improvement, especially in directional sea states.

We thus addressed an explicit formulation of the complementary ICWM (CICWM) with the nonlinear terms for free surface elevation in directional wave fields. To the best of the authors' knowledge, a Lagrangian model with second-order nonlinear interactions within a formalism of free surface elevation has not been developed previously. We also derived simplified ICWM (SICWM) that falls between ICWM and the linear wave theory model with a corrected dispersion relationship (LWT-CDR). Lastly, we established a hierarchy of wave models from LWT to CICWM, ordered by their development of nonlinear aspects.

Formulations for data assimilation (or reconstruction, referred to as 'nowcast') and wave propagation (or prediction, referred to as 'forecast') have been detailed for all the models. Previously, the inclusion of second-order Lagrangian nonlinear interaction terms was deemed prohibitive for real-time applications. However, we have successfully provided real-time wave forecasting for multidirectional seas using a simplified assimilation method suggested in Kim et al. (2023a). In Table 2, wave prediction for all the models was confirmed to be completed within a few seconds or less, enabling real-time prediction for actual sea states with a prediction horizon of approximately 20 s in the configuration tested here.

Comparing the model performances against dedicated tank-scale experiments demonstrated that the second-order nonlinear interaction terms in CICWM enhance the description of surface elevation more in directional sea states than in unidirectional sea states. Notably, for the experimental setups and sea states investigated in this study, it was observed that the second-order Lagrangian wave model can reduce the prediction error of the linear wave model by 90% even in directional seas. Future research may explore expanding the model to address ocean engineering challenges with a larger distance of a point of interest from the observation zone or for long-term wave predictions.

CRediT authorship contribution statement

I.-C. Kim: Writing – original draft, Visualization, Validation, Software, Methodology, Investigation, Conceptualization. **G. Ducrozet:** Writing – review & editing, Supervision, Project administration, Methodology, Investigation, Conceptualization.

Declaration of competing interest

The authors declare that they have no known competing financial interests or personal relationships that could have appeared to influence the work reported in this paper.

Data availability

The experimental datasets and wave prediction results are openly available at https://doi.org/10.5281/zenodo.7689781 repository.

Acknowledgments

This work was done within the framework of the European H2020 FLOATECH project, Grant agreement ID: 101007142. The authors acknowledge the support of the French Agence Nationale de la Recherche (ANR), under grant ANR-20-CE05-0039 (project CREATIF).

The authors also thank the experimental team at LHEEA/Centrale Nantes-CNRS who contributed to the experimental campaign and the corresponding database.

Appendix A. Derivation of SICWM

The surface elevation form of SICWM (Eq. (25)) can be obtained through a simplification of the one formulated with ICWM (Eq. (26)). The entire derivation is given in this appendix.

First, the nonlinear phase function Ψ_i can be expressed with the modified phase function $\tilde{\psi}_i$ and the nonlinear phase shift $\mathbf{D}$:

$$\Psi_i = \tilde{\psi}_i - \mathbf{k}_i \cdot \mathbf{D} \tag{A.1}$$

with

$$\mathbf{D} = \sum_{i=1}^{N} \hat{\mathbf{k}}_i(-a_i \sin\tilde{\psi}_i + b_i \cos\tilde{\psi}_i) \tag{A.2}$$

The surface elevation by ICWM (Eq. (26)) is expanded in a Taylor expansion around $\tilde{\psi}_i$:

$$\begin{aligned}\eta(x,y,t) = &\sum_{i=1}^{N}[a_i\cos\tilde{\psi}_i + b_i\sin\tilde{\psi}_i] \\ &+ \sum_{i=1}^{N}[\mathbf{k}_i\cdot\mathbf{D}(a_i\sin\tilde{\psi}_i - b_i\cos\tilde{\psi}_i) + \frac{1}{2}({a_i}^2 + {b_i}^2)k_i]\end{aligned} \tag{A.3}$$

where the effect of the nonlinear phase shift $\mathbf{D}$ is expressed as the interactions between two arbitrary modes. As in the derivation of ICWM, we only include the interaction between identical wave modes:

$$\begin{aligned}\eta(x,y,t) = &\sum_{i=1}^{N}[a_i\cos\tilde{\psi}_i + b_i\sin\tilde{\psi}_i] \\ &+ \sum_{i=1}^{N}[-(a_i\sin\tilde{\psi}_i - b_i\cos\tilde{\psi}_i)^2 k_i + \frac{1}{2}({a_i}^2 + {b_i}^2)k_i]\end{aligned} \tag{A.4}$$

Here, it is confirmed that the second-order mean vertical level introduced to have the zero-mean level (i.e., the last term in Eq. (A.4))

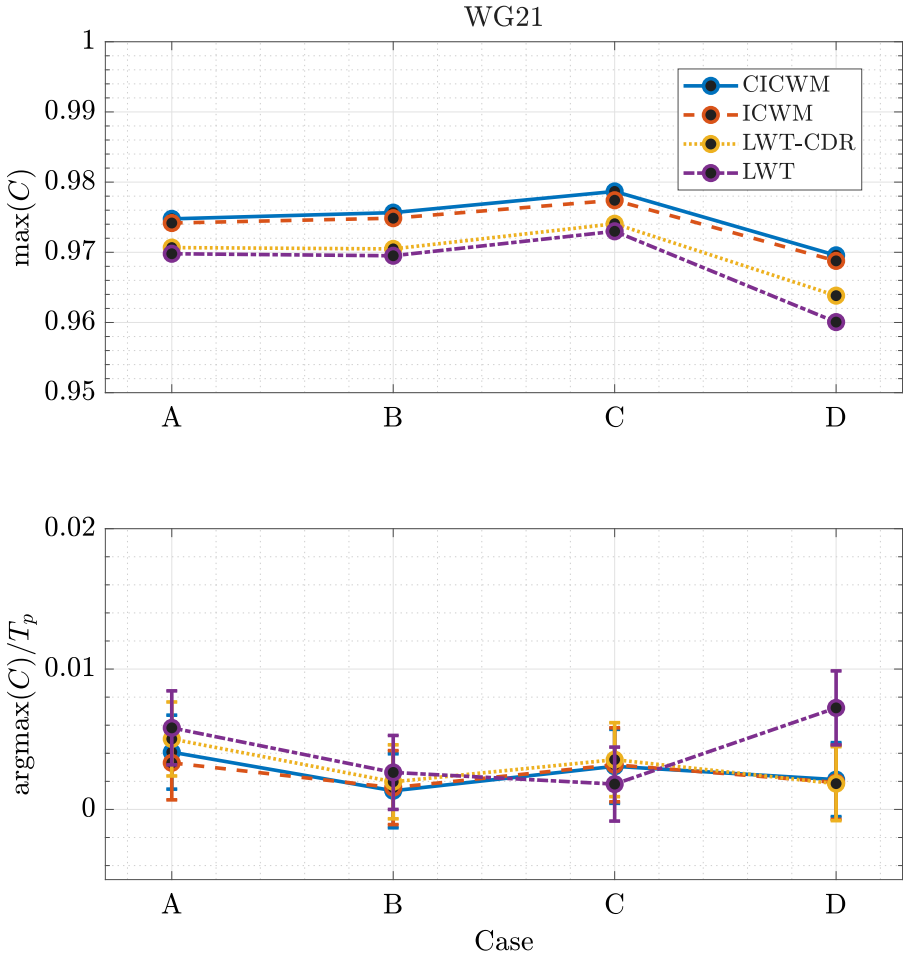

Fig. 10. Cross-correlation between predicted and measured surface elevations at WG21: (a) maximum value; (b) corresponding normalized time-lag (——: CICWM; – – : ICWM; ·····: LWT-CDR; —·—: LWT).

is canceled out, such that we reach the zero mean. Lastly, Eq. (A.4) can be arranged in the final form of CICWM:

$$\eta(x,y,t) = \sum_{i=1}^{N}[a_i\cos\tilde{\psi}_i + b_i\sin\tilde{\psi}_i] + \frac{1}{2}\sum_{i=1}^{N}[({a_i}^2 - {b_i}^2)k_i\cos 2\tilde{\psi}_i + 2a_ib_ik_i\sin 2\tilde{\psi}_i] \tag{A.5}$$

Appendix B. Formulations in data assimilation

Section 3.2 explained data assimilation for wave reconstruction based on wave measurement data. Here, we provide the remaining details. The coefficient matrix **A** is composed of $A_{(m,n)}$, $A_{(m,N+n)}$, $A_{(N+m,n)}$, and $A_{(N+m,N+n)}$, while the observation vector **B** is composed of B_m and B_{N+m}.

The coefficients of the matrix **A** for SICWM are given by:

$$\begin{aligned}
A^{SICWM}_{(m,n)} &= \sum_{l=1}^{L}(\cos\tilde{\psi}_{nl} + \frac{a_nk_n}{2}\cos 2\tilde{\psi}_{nl} + \frac{b_nk_n}{2}\sin 2\tilde{\psi}_{nl})P^{LWT}_{ml}\\
A^{SICWM}_{(m,N+n)} &= \sum_{l=1}^{L}(\sin\tilde{\psi}_{nl} + \frac{a_nk_n}{2}\sin 2\tilde{\psi}_{nl} - \frac{b_nk_n}{2}\cos 2\tilde{\psi}_{nl})P^{LWT}_{ml}\\
A^{SICWM}_{(N+m,n)} &= \sum_{l=1}^{L}(\cos\tilde{\psi}_{nl} + \frac{a_nk_n}{2}\cos 2\tilde{\psi}_{nl} + \frac{b_nk_n}{2}\sin 2\tilde{\psi}_{nl})Q^{LWT}_{ml}\\
A^{SICWM}_{(N+m,N+n)} &= \sum_{l=1}^{L}(\sin\tilde{\psi}_{nl} + \frac{a_nk_n}{2}\sin 2\tilde{\psi}_{nl} - \frac{b_nk_n}{2}\cos 2\tilde{\psi}_{nl})Q^{LWT}_{ml}
\end{aligned} \tag{B.1}$$

The coefficients of the matrix **A** for ICWM are given by:

$$\begin{aligned}
A^{ICWM}_{(m,n)} &= \sum_{l=1}^{L}(\cos\Psi_{nl} + \frac{a_nk_n}{2})P^{LWT}_{ml}\\
A^{ICWM}_{(m,N+n)} &= \sum_{l=1}^{L}(\sin\Psi_{nl} + \frac{b_nk_n}{2})P^{LWT}_{ml}\\
A^{ICWM}_{(N+m,n)} &= \sum_{l=1}^{L}(\cos\Psi_{nl} + \frac{a_nk_n}{2})Q^{LWT}_{ml}\\
A^{ICWM}_{(N+m,N+n)} &= \sum_{l=1}^{L}(\sin\Psi_{nl} + \frac{b_nk_n}{2})Q^{LWT}_{ml}
\end{aligned} \tag{B.2}$$

where $\Psi_{ml} = \mathbf{k}_{ml}\cdot[\mathbf{r}_l - \sum_{i=1}^{N}(-a_i\sin\tilde{\psi}_{il} + b_i\cos\tilde{\psi}_{il})] - \tilde{\omega}_m t_l$.

The coefficients of the matrix **A** for CICWM are given by:

$$\begin{aligned}
A^{CICWM}_{(m,n)} &= A^{ICWM}_{(m,n)} + \sum_{l=1}^{L}\left(\sum_{\substack{j_\omega\geq i_\omega\\ j_\theta\geq i_\theta}}\begin{bmatrix} CIC^1_{nj}\left(a_j\cos\Psi_{jl} + b_j\sin\Psi_{jl}\right)\cos\Psi_{nl}\\ +CIC^2_{nj}\left(a_j\sin\Psi_{jl} - b_j\cos\Psi_{jl}\right)\sin\Psi_{nl}\end{bmatrix}\right)P^{LWT}_{ml}\\
A^{CICWM}_{(m,N+n)} &= A^{ICWM}_{(m,N+n)} + \sum_{l=1}^{L}\left(\sum_{\substack{j_\omega\geq i_\omega\\ j_\theta\geq i_\theta}}\begin{bmatrix} CIC^1_{nj}\left(a_j\cos\Psi_{jl} + b_j\sin\Psi_{jl}\right)\sin\Psi_{nl}\\ -CIC^2_{nj}\left(a_j\sin\Psi_{jl} - b_j\cos\Psi_{jl}\right)\cos\Psi_{nl}\end{bmatrix}\right)P^{LWT}_{ml}\\
A^{CICWM}_{(N+m,n)} &= A^{ICWM}_{(m,N+n)} + \sum_{l=1}^{L}\left(\sum_{\substack{j_\omega\geq i_\omega\\ j_\theta\geq i_\theta}}\begin{bmatrix} CIC^1_{nj}\left(a_j\cos\Psi_{jl} + b_j\sin\Psi_{jl}\right)\cos\Psi_{nl}\\ +CIC^2_{nj}\left(a_j\sin\Psi_{jl} - b_j\cos\Psi_{jl}\right)\sin\Psi_{nl}\end{bmatrix}\right)Q^{LWT}_{ml}\\
A^{CICWM}_{(N+m,N+n)} &= A^{ICWM}_{(N+m,N+n)} + \sum_{l=1}^{L}\left(\sum_{\substack{j_\omega\geq i_\omega\\ j_\theta\geq i_\theta}}\begin{bmatrix} CIC^1_{nj}\left(a_j\cos\Psi_{jl} + b_j\sin\Psi_{jl}\right)\sin\Psi_{nl}\\ -CIC^2_{nj}\left(a_j\sin\Psi_{jl} - b_j\cos\Psi_{jl}\right)\cos\Psi_{nl}\end{bmatrix}\right)Q^{LWT}_{ml}
\end{aligned} \tag{B.3}$$

where the combinations of the interaction coefficients CIC^1_{nj} and CIC^1_{nj} can be obtained by adjusting Eqs. (21) and (22). Following Kim et al. (2024a), the iterative process was conducted with a maximum iteration number of 20 and a tolerance of 10^{-2}, with the initial amplitude parameter guess obtained from the previous surface sample.

References

Al, M., Fontanella, A., van der Hoek, D., Liu, Y., Belloli, M., van Wingerden, J.-W., 2020. Feedforward control for wave disturbance rejection on floating offshore wind turbines. J. Phys.: Conf. Ser. 1618 (2), 022048.

Belmont, M., 2023. Wave shadowing effects on phase resolved wave spectra estimated from radar backscatter: Part 2: The conflation technique and the deconvolution techniques for the mitigation of wave shadowing effects. Ocean Eng. 267, 113315.

Belmont, M., Horwood, J., Thurley, R., Baker, J., 2007. Shallow angle wave profiling lidar. J. Atmos. Ocean. Technol. 24 (6), 1150–1156.

Blondel, E., Bonnefoy, F., Ferrant, P., 2010. Deterministic non-linear wave prediction using probe data. Ocean Eng. 37 (10), 913–926.

Bonnefoy, F., Delacroix, S., Ducrozet, G., Kim, I., Leroy, V., 2023. FLOATECH Project Database. Zenodo, http://dx.doi.org/10.5281/zenodo.7689781, Funded by European Commission, project FLOATECH, grant 101007142.

Clamond, D., 2007. On the Lagrangian description of steady surface gravity waves. J. Fluid Mech. 589, 433–454.

Dannenberg, J., Hessner, K., Naaijen, P., van den Boom, H., Reichert, K., 2010. The on board wave and motion estimator OWME. In: The Twentieth International Offshore and Polar Engineering Conference. OnePetro, pp. 424–431.

Desmars, N., Bonnefoy, F., Grilli, S., Ducrozet, G., Perignon, Y., Guérin, C.-A., Ferrant, P., 2020. Experimental and numerical assessment of deterministic nonlinear ocean waves prediction algorithms using non-uniformly sampled wave gauges. Ocean Eng. 212, 107659.

Desmars, N., Hartmann, M., Behrendt, J., Hoffmann, N., Klein, M., 2023. Nonlinear deterministic reconstruction and prediction of remotely measured ocean surface waves. J. Fluid Mech. 975, A8.

Gerstner, F., 1809. Theorie der wellen. Ann. Phys., Lpz. 32 (8), 412–445.

Grilli, S.T., Guérin, C.-A., Goldstein, B., 2011. Oceanwave reconstruction algorithms based on spatio-temporal data acquired by a flash LiDAR camera. In: The Twenty-First International Offshore and Polar Engineering Conference. OnePetro, pp. 275–282.

Guérin, C.-A., Desmars, N., Grilli, S.T., Ducrozet, G., Perignon, Y., Ferrant, P., 2019. An improved Lagrangian model for the time evolution of nonlinear surface waves. J. Fluid Mech. 876, 527–552.

Guo, B., Patton, R., Jin, S., 2017. Identification and validation of excitation force for a heaving point absorber wave energy convertor. Proc. EWTEC 1–9.

Hilmer, T., Thornhill, E., 2015. Observations of predictive skill for real-time deterministic sea waves from the WaMoS II. In: OCEANS 2015-MTS/IEEE Washington. IEEE, pp. 1–7.

Janssen, T., Herbers, T., Battjes, J., 2006. Generalized evolution equations for nonlinear surface gravity waves over two-dimensional topography. J. Fluid Mech. 552, 393–418.

Kabel, T., Georgakis, C.T., Zeeberg, A.R., 2019. Mapping ocean waves using new LIDAR equipment. In: Proceedings of the Twenty-Ninth (2019) International Ocean and Polar Engineering Conference. nternational Society of Offshore and Polar Engineers, pp. 2258–2562.

Kim, I.-C., Ducrozet, G., Bonnefoy, F., Leroy, V., Perignon, Y., 2023a. Real-time phase-resolved ocean wave prediction in directional wave fields: Enhanced algorithm and experimental validation. Ocean Eng. 276, 114212.

Kim, I.-C., Ducrozet, G., Leroy, V., Bonnefoy, F., Perignon, Y., Bourguignon, S., 2024a. A real-time wave prediction in directional wave fields: Strategies for accurate continuous prediction in time. Ocean Eng. 291, 116445.

Kim, I.-C., Ducrozet, G., Leroy, V., Bonnefoy, F., Perignon, Y., Delacroix, S., 2024b. Numerical and experimental investigation on deterministic prediction of ocean surface wave and wave excitation force. Appl. Ocean Res. 142, 103834.

Kim, I.-C., Ducrozet, G., Perignon, Y., 2023b. Development of phase-resolved real-time wave forecasting with unidirectional and multidirectional seas. In: ASME 2023 42nd International Conference on Ocean, Offshore and Arctic Engineering. American Society of Mechanical Engineers Digital Collection, V005T06A104.

Klein, M., Dudek, M., Clauss, G.F., Ehlers, S., Behrendt, J., Hoffmann, N., Onorato, M., 2020. On the deterministic prediction of water waves. Fluids 5 (1), 9.

Kusters, J., Cockrell, K., Connell, B., Rudzinsky, J., Vinciullo, V., 2016. FutureWaves™: A real-time ship motion forecasting system employing advanced wave-sensing radar. In: OCEANS 2016 MTS/IEEE Monterey. IEEE, pp. 1–9.

Lamb, H., 1932. Hydrodynamics. Cambridge University Press/Dover.

Li, G., Weiss, G., Mueller, M., Townley, S., Belmont, M.R., 2012. Wave energy converter control by wave prediction and dynamic programming. Renew. Energy 48, 392–403.

Lindgren, G., 2006. Slepian models for the stochastic shape of individual Lagrange sea waves. Adv. in Appl. Probab. 38 (2), 430–450.

Lindgren, G., Åberg, S., 2009. First order stochastic Lagrange model for asymmetric ocean waves. J. Offshore Mech. Arct. Eng. 131 (3), 031602.

Longuet-Higgins, M.S., 1963. The effect of non-linearities on statistical distributions in the theory of sea waves. J. Fluid Mech. 17 (3), 459–480.
Ma, Y., Sclavounos, P.D., Cross-Whiter, J., Arora, D., 2018. Wave forecast and its application to the optimal control of offshore floating wind turbine for load mitigation. Renew. Energy 128, 163–176.
Mitsuyasu, H., Tasai, F., Suhara, T., Mizuno, S., Ohkusu, M., Honda, T., Rikiishi, K., 1975. Observations of the directional spectrum of ocean WavesUsing a cloverleaf buoy. J. Phys. Oceanogr. 5 (4), 750–760.
Naaijen, P., Trulsen, K., Blondel-Couprie, E., 2014. Limits to the extent of the spatio-temporal domain for deterministic wave prediction. Int. Shipbuild. Prog. 61 (3–4), 203–223.
Naaijen, P., Van Oosten, K., Roozen, K., van't Veer, R., 2018. Validation of a deterministic wave and ship motion prediction system. In: International Conference on Offshore Mechanics and Arctic Engineering. vol. 51272, American Society of Mechanical Engineers, V07BT06A032.
Nouguier, F., Chapron, B., Guérin, C.-A., 2015. Second-order Lagrangian description of tri-dimensional gravity wave interactions. J. Fluid Mech. 772, 165–196.
Nouguier, F., Grilli, S.T., Guérin, C.-A., 2013. Nonlinear ocean wave reconstruction algorithms based on simulated spatiotemporal data acquired by a flash LIDAR camera. IEEE Trans. Geosci. Remote Sens. 52 (3), 1761–1771.
Nouguier, F., Guérin, C.-A., Chapron, B., 2009. "Choppy wave" model for nonlinear gravity waves. J. Geophys. Res. 114 (C9).
Nouguier, F., Guérin, C.-A., Chapron, B., 2010. Scattering from nonlinear gravity waves: The "choppy wave" model. IEEE Trans. Geosci. Remote Sens. 48 (12), 4184–4192.
Pierson, Jr., W.J., 1961. Models of Random Seas Based on the Lagrangian Equations of Motion. Technical Report, New York Univ Bronx School of Engineering and Science.
Pierson, Jr., W.J., Moskowitz, L., 1964. A proposed spectral form for fully developed wind seas based on the similarity theory of SA kitaigorodskii. J. Geophys. Res. 69 (24), 5181–5190.
Previsic, M., Karthikeyan, A., Lyzenga, D., 2021. In-ocean validation of a deterministic sea wave prediction (DSWP) system leveraging X-band radar to enable optimal control in wave energy conversion systems. Appl. Ocean Res. 114, 102784.
Raach, S., Schlipf, D., Sandner, F., Matha, D., Cheng, P.W., 2014. Nonlinear model predictive control of floating wind turbines with individual pitch control. In: 2014 American Control Conference. IEEE, pp. 4434–4439.
Simpson, A., Haller, M., Walker, D., Lynett, P., Honegger, D., 2020. Wave-by-wave forecasting via assimilation of marine radar data. J. Atmos. Ocean. Technol. 37 (7), 1269–1288.
Socquet-Juglard, H., Dysthe, K., Trulsen, K., Krogstad, H.E., Liu, J., 2005. Probability distributions of surface gravity waves during spectral changes. J. Fluid Mech. 542, 195–216.
Stoker, J.J., 1992. Water Waves: The Mathematical Theory with Applications, vol. 36, John Wiley & Sons.
Tanaka, M., 2001. Verification of Hasselmann's energy transfer among surface gravity waves by direct numerical simulations of primitive equations. J. Fluid Mech. 444, 199–221.
Taylor, K.E., 2001. Summarizing multiple aspects of model performance in a single diagram. J. Geophys. Res. 106 (D7), 7183–7192.
Zhang, C., Chen, Z., Zhao, C., Chen, X., Wei, Y., He, J., 2022. Deterministic sea wave prediction based on least squares with regularization algorithm using coherent microwave radar. IEEE Trans. Geosci. Remote Sens..